Check for updates

JAMES | Journal of Advances in Modeling Earth Systems

RESEARCH ARTICLE
10.1029/2023MS003632

Improving Stratocumulus Cloud Amounts in a 200-m Resolution Multi-Scale Modeling Framework Through Tuning of Its Interior Physics

Liran Peng[1], Peter N. Blossey[2], Walter M. Hannah[3], Christopher S. Bretherton[2,4], Christopher R. Terai[3], Andrea M. Jenney[1], and Michael Pritchard[1,5]

[1]Department of Earth System Science, University of California, Irvine, Irvine, CA, USA, [2]Department of Atmospheric Sciences, University of Washington, Seattle, WA, USA, [3]Lawrence Livermore National Laboratory, Livermore, CA, USA, [4]Allen Institute for Artificial Intelligence, Seattle, WA, USA, [5]NVIDIA, Santa Clara, CA, USA

Abstract High-Resolution Multi-scale Modeling Frameworks (HR)—global climate models that embed separate, convection-resolving models with high enough resolution to resolve boundary layer eddies—have exciting potential for investigating low cloud feedback dynamics due to reduced parameterization and ability for multidecadal throughput on modern computing hardware. However low clouds in past HR have suffered a stubborn problem of over-entrainment due to an uncontrolled source of mixing across the marine subtropical inversion manifesting as stratocumulus dim biases in present-day climate, limiting their scientific utility. We report new results showing that this over-entrainment can be partly offset by using hyperviscosity and cloud droplet sedimentation. Hyperviscosity damps small-scale momentum fluctuations associated with the formulation of the momentum solver of the embedded large eddy simulation. By considering the sedimentation process adjacent to default one-moment microphysics in HR, condensed phase particles can be removed from the entrainment zone, which further reduces entrainment efficiency. The result is an HR that can produce more low clouds with a higher liquid water path and a reduced stratocumulus dim bias. Associated improvements in the explicitly simulated sub-cloud eddy spectrum are observed. We report these sensitivities in multi-week tests and then explore their operational potential alongside microphysical retuning in decadal simulations at operational 1.5° exterior resolution. The result is a new HR having desired improvements in the baseline present-day low cloud climatology, and a reduced global mean bias and root mean squared error of absorbed shortwave radiation. We suggest it should be promising for examining low cloud feedbacks with minimal approximation.

Plain Language Summary Stratocumulus clouds cover a large fraction of the globe but are very challenging to reproduce in computer simulations of Earth's atmosphere because of their unique complexity. Previous studies find the model produces too few Stratocumulus clouds as we increase the model resolution, which, in theory, should improve the simulation of important motions for the clouds. This is because the clouds are exposed to more conditions that make them evaporate away. On Earth, stratocumulus clouds reflect a lot of sunlight. In the computer model of Earth, too much sunlight reaches the surface because of too few stratocumulus clouds, which makes it warmer. This study tests two methods to thicken Stratocumulus clouds in the computer model Earth. The first method smooths out some winds, which helps reduce the exposure of clouds to the conditions that make them evaporate. The second method moves water droplets in the cloud away from the conditions that would otherwise make them evaporate. In long simulations, combining these methods helps the model produce thicker stratocumulus clouds with more water.

Key Points:

- We improve a long-standing stratocumulus (Sc) dim bias in a high-resolution Multiscale Modeling Framework
- Incorporating intra-CRM hyperviscosity hedges against the numerics of its momentum solver, reducing entrainment vicinity
- Further adding sedimentation boosts Sc brightness close to observed, opening path to more faithful low cloud feedback analysis

Correspondence to:
L. Peng,
liranp@uci.edu

Citation:
Peng, L., Blossey, P. N., Hannah, W. M., Bretherton, C. S., Terai, C. R., Jenney, A. M., & Pritchard, M. (2024). Improving stratocumulus cloud amounts in a 200-m resolution multi-scale modeling framework through tuning of its interior physics. *Journal of Advances in Modeling Earth Systems*, *16*, e2023MS003632. https://doi.org/10.1029/2023MS003632

Received 2 FEB 2023
Accepted 20 FEB 2024

Author Contributions:
Conceptualization: Liran Peng, Peter N. Blossey, Christopher S. Bretherton, Christopher R. Terai, Andrea M. Jenney, Michael Pritchard
Data curation: Walter M. Hannah
Formal analysis: Liran Peng, Peter N. Blossey, Walter M. Hannah, Christopher S. Bretherton, Andrea M. Jenney, Michael Pritchard
Funding acquisition: Peter N. Blossey
Investigation: Liran Peng, Walter M. Hannah, Christopher S. Bretherton, Andrea M. Jenney, Michael Pritchard
Methodology: Liran Peng, Peter N. Blossey, Walter M. Hannah, Christopher S. Bretherton, Andrea M. Jenney, Michael Pritchard

© 2024 The Authors. Journal of Advances in Modeling Earth Systems published by Wiley Periodicals LLC on behalf of American Geophysical Union.
This is an open access article under the terms of the Creative Commons Attribution License, which permits use, distribution and reproduction in any medium, provided the original work is properly cited.

1. Introduction

Stratocumulus (Sc) clouds play an important role in the Earth's radiation budget. They are extensive, long-lived, and cool the Earth by reflecting downwelling solar radiation back to space while having little impact on the outgoing longwave radiation. Primarily formed in the presence of large-scale subsidence over cold oceans, the annual mean Sc coverage over the ocean and land is 23% and 12%, respectively (Wood, 2012). Sc also has a strong influence on the heat and moisture exchange between the troposphere and boundary layer (Randall et al., 1984). Despite the climatic significance of Sc, climate models do not agree on their seasonal cycle, spatial extent, radiative properties, and cloud feedbacks (Bony et al., 2011; Brunke et al., 2019; Gettelman & Sherwood, 2016; Konsta et al., 2022; Lin et al., 2014; Tselioudis et al., 2021; Vignesh et al., 2020; Zelinka

Project administration: Michael Pritchard
Resources: Liran Peng, Peter N. Blossey, Walter M. Hannah
Supervision: Michael Pritchard
Validation: Liran Peng, Christopher S. Bretherton, Michael Pritchard
Visualization: Liran Peng, Walter M. Hannah
Writing – original draft: Liran Peng
Writing – review & editing: Liran Peng, Peter N. Blossey, Walter M. Hannah, Christopher S. Bretherton, Christopher R. Terai, Andrea M. Jenney, Michael Pritchard

et al., 2022), and even high resolution models simulate widely varying cloud properties in idealized case studies (Ackerman et al., 2009; Bretherton et al., 1999; Stevens et al., 2005). More realistic simulated Sc is necessary to improve our understanding of Sc physics and confidence in projections of the future global-mean temperature (Bony & Dufresne, 2005; Dal Gesso et al., 2015; Schneider et al., 2017; Tsushima et al., 2016; Webb et al., 2013; Zelinka et al., 2020).

Simulating Sc remains a particular challenge because Sc processes involve a wide range of spatial scales and key physical processes that are poorly represented in the subgrid-scale parameterization of global models. Although an Sc cloud deck might cover tens to thousands of kilometers, its thickness is typically only a few hundred meters (Wood, 2012). Cloud-aerosol interactions are modulated through changes in cloud droplet number, which itself depends on the strength of updrafts whose scale is on the order of 10s or 100s of meters. At the top of subtropical stratocumulus clouds, intense mixing between warm, dry free-tropospheric air and the underlying wet cloud layer occurs within a thin layer typically less than 20 m in vertical extent (Caughey et al., 1982; Haman et al., 2007; Mellado, 2017). Bretherton (2015) suggests that such cloud-top entrainment plays a leading role in multiple cloud feedback mechanisms in stratocumulus. Because low cloud feedbacks and cloud-aerosol interactions in stratocumulus clouds are thought to be controlled in part by fine-scale processes that are not represented explicitly in storm-resolving models (∼1 km), this motivates simulations with sub-kilometer grid spacing (e.g., Stevens et al., 2020).

Several interesting strategies have emerged in recent years to capture more explicit and plausible stratocumulus dynamics in next generation global climate models. First, Lee et al. (2022) demonstrate some potential from adaptively refining vertical grid structure solely within a strategic subset of the physical parameterization suite, with higher order closure scheme used in Cloud Layers Unified By-Binormals (CLUBB, Golaz et al., 2002a, 2002b; Larson & Golaz, 2005; Larson et al., 2012) and vertical transport (e.g., subsidence and sedimentation/precipitation). This has advantages of producing some better baseline Sc (Bogenschutz et al., 2013; Lee et al., 2022), but disadvantages of accepting all the limitations of operational subgridscale turbulence schemes. Second, (Lopez-Gomez et al., 2020) sidesteps the turbulence parameterization problem by using very highly resolved ($\Delta x = \Delta y = 35$ m and $\Delta z = 5$ m) three dimensional LES, managing computational expense by using a sparse ensemble as a library from which to train eddy diffusivity/mass flux based parameterization schemes (Cohen et al., 2020). Advantages of the highly resolved LES choice include a luxuriously converged limit that sidesteps most need to parameterize beyond microphysics; disadvantages include imposing idealizations of lateral periodicity and a scale separation in their harness to a global host, as well as limited geographic sampling due to the expense of such LES; however, the latter is positioned to be managed with calibration schemes that may inform where such calculations can be strategically deployed to maximum global benefit (Dunbar et al., 2022). Advantages of the Eddy-Diffusivity Mass-Flux (EDMF) framework include its interpretability and generalizability; disadvantages include its potential inability to subsume some complicated organization feedbacks. Finally, Miyamoto et al. (2013) avoids scale separations entirely by directly resolving fully global uniform 870-m horizontal resolution. Similar work currently planned to attain 200-m global horizontal resolution has advantages of resolving the outer scale of boundary layer eddies without drawing scale separations, but the disadvantage of the inordinate computational expense and inability to conduct multidecadal cloud feedback experiments, as well as a limited ability to refine vertical grids near the inversion. All of the above approaches must cope with the ongoing difficulties and uncertainty of how to parameterize microphysics.

We will focus on a strategy that is complementary to all the above approaches for dealing with the computational challenge of low clouds for climate simulation, by using the multiscale modeling framework (MMF, also referred to as "superparameterization (SP)"; Grabowski (2004), M. F. Khairoutdinov and Randall (2001), and W. M. Hannah et al. (2020)), in which a coarse resolution (∼100 km) global climate model (GCM) is coupled to an embedded convection-resolving models (CRMs) at each global grid location. Many previous studies (Kooperman et al., 2016a, 2016b) have shown low-resolution MMF (LR) tests with a traditional MMF, that is, using coarse 4-km horizontal resolution and greater than 100-m vertical spacing, can improve the simulated rainfall distribution and wave spectrum near the equator and over summer continents. However low-cloud-forming eddies are not directly resolved in this approach, requiring subgrid scale parameterizations to cope with (Cheng & Xu, 2015; Wang et al., 2015).

19422466, 2024, 3, Downloaded from https://agupubs.onlinelibrary.wiley.com/doi/10.1029/2023MS003632 by University Of Washington, Wiley Online Library on [25/09/2024]. See the Terms and Conditions (https://onlinelibrary.wiley.com/terms-and-conditions) on Wiley Online Library for rules of use; OA articles are governed by the applicable Creative Commons License

19422466, 2024, 3, Downloaded from https://agupubs.onlinelibrary.wiley.com/doi/10.1029/2023MS003632 by University Of Washington, Wiley Online Library on [25/09/2024]. See the Terms and Conditions (https://onlinelibrary.wiley.com/terms-and-conditions) on Wiley Online Library for rules of use; OA articles are governed by the applicable Creative Commons License

The MMF coupling paradigm does not put constraints on the CRM domain size or grid spacing, so large eddy permitting resolution can be used to sidestep most of the parameterization problem regarding cloud-forming eddies. The MMF approach makes the physical idealizations of imposing lateral periodicity in the CRM and a scale separation between the GCM and CRM, and historically has limited the CRM to just two dimensions for computational efficiency. Despite these concessions the MMF has a unique computational advantage that enables full geographic sampling and relatively fast throughput, with options to accelerate the CRM algorithmically (Jones et al., 2015) or via GPU hardware (W. M. Hannah et al., 2020), and regionalized load balancing (Peng et al., 2022) that makes the MMF approach increasingly attractive for climate dynamics and low cloud feedback applications.

A high-resolution MMF (HR) with a grid designed for low cloud simulations was first explored by Parishani et al. (2017) with hopes of more directly simulating shallow convection over Sc-covered regions. Encouraging initial improvements in low cloud vertical structure, diurnal sensitivity, and the vertical structure of sub-cloud turbulent kinetic energy were reported in a model configuration using simplified bulk, one-moment cloud microphysics.

However, such HR experiments have to date been unable to sustain sufficient liquid water in stratocumulus regions, where simulations suffer from an undesired regional dim bias that has been difficult to overcome (Parishani et al., 2017). Associated symptoms have implicated an unknown source of vertical mixing that disrupts the balance required to sustain morning Sc by mixing too much free tropospheric air into the boundary layer. The overall impact is to under-predict daytime cloud liquid water resulting in too little time mean shortwave reflectivity. Meanwhile, the assumptions inherent in an MMF that can limit its ability to laterally advect condensed water between adjacent CRMs have caused some to question its capacity to maintain low clouds (Jansson et al., 2022). While the scale separation inherent in the MMF also introduces distortions (such as the neglect of the mesoscale), it does allow a global model to simulate these fine scales, making it possible to represent physical processes (e.g., cloud top entrainment, aerosol activation in updrafts) that drive critical sensitivities of low clouds to anthropogenic influence.

In short, the question is open as to whether the HR approach should ever be expected to maintain realistic amounts of liquid in marine Sc regions, to the extent that it must rely primarily on local cloud generation to succeed, and given that over-entrainment has proved a stubborn problem to overcome. Motivated by the Transpose-Atmospheric Model Intercomparison Project (Transpose-AMIP, Williams et al., 2013), we use the hindcast approach to test different model configurations. In this context, the purpose of this paper is to explore two mechanisms to control entrainment efficiency in a HR and examine the extent to which they can alleviate the Sc dim bias issue. The first is to numerically damp unphysical noise at the grid scale caused by the numerics by applying a hyperdiffusive term (which we will refer to as "hyperviscosity") to the momentum equation that can reduce entrainment and entrainment efficiency (Wyant et al., 2018). Second, enhancing cloud droplet sedimentation (henceforth, "sedimentation"), which can also reduce the entrainment efficiency and preserve cloud liquid by depleting the liquid water in the cloud-top entrainment zone (Bretherton et al., 2007). We will use the term "entrainment efficiency" in our study as an indicator of the magnitude of tendencies resulting from the combined effects of explicitly resolved mixing, numerical diffusion, and parameterized subgrid-scalediffusion.

The paper is organized as follows: Section 2 contains a rationale and description of how we implement both hyperviscosity and sedimentation processes. In Section 3, we first analyze the results of six, short-duration sensitivity simulations in a testbed HR configuration to understand the impact of varying degrees of CRM-scale hyperviscosity and sedimentation on low cloud characteristics and the spectrum of turbulent eddies in the marine boundary layer. These results point to temporal nonlinearities and a promising configuration for longer-duration simulations in an operational configuration, for which we show results from a subsequent round of microphysical tunings. This allows an updated view of HR top of atmosphere radiative biases after controlling for over-entrainment. A summary of the results and a discussion are included in Section 4.

2. Methods

2.1. Model Description

In this study, we use the Multi-scale Modeling Framework configuration of the Energy Exascale Earth System Model (E3SM-MMF; W. M. Hannah et al., 2020) as a testbed to examine the impact of hyperviscosity and

19422466, 2024, 3, Downloaded from https://agupubs.onlinelibrary.wiley.com/doi/10.1029/2023MS003632 by University Of Washington, Wiley Online Library on [25/09/2024]. See the Terms and Conditions (https://onlinelibrary.wiley.com/terms-and-conditions) on Wiley Online Library for rules of use; OA articles are governed by the applicable Creative Commons License

sedimentation on low clouds simulated by high resolution embedded convection arrays. E3SM was forked from the NCAR CESM (Hurrell et al., 2013) but has undergone continued development and enhancement since then (Golaz et al., 2019; Xie et al., 2018). The dynamical core uses a spectral element method on a cubed-sphere geometry (Ronchi et al., 1996; Taylor et al., 2007). Physics calculations are done on a finite volume grid that is slightly coarser than the spectral element grid used for dynamics, but the physics grid is comparable to the effective resolution of the dynamics grid and does not alter the qualitative behavior of the model (W. M. Hannah et al., 2021).

Each simulation follows the approach of (M. Khairoutdinov et al., 2005) with a two-dimensional CRM based on the System for Atmospheric Modeling (SAM, M. Khairoutdinov et al., 2005) embedded within each GCM physics column. These embedded CRMs are oriented meridionally within the host GCM grid cell and have periodic lateral boundary conditions. The vertical grid and background anelastic state are updated to match the parent GCM column for each CRM integration (typically once per GCM time step). The CRM uses a one-moment microphysics scheme with a temperature-dependent partitioning of the cloud condensate (cloud water and ice) and a subgrid-scale (SGS) turbulent transport scheme with a diagnostic Smagorinsky closure. The rapid radiative transfer model for General model application (RRTMGP) (Pincus et al., 2019) is used for radiation, which has been rewritten in C++ to run efficiently on GPUs. CRM columns are combined for radiative calculations to reduce the computational burden of radiation instead of considering each CRM column separately, which does not qualitatively affect the model solution for typical configurations with four or more radiative columns. Radiative tendencies are calculated once each GCM time step and are applied back to the corresponding group of CRM columns on the following time step. The domain average CRM variables for temperature and water species are used to calculate forcing and feedback tendencies in order to couple the CRM and GCM, following the conventional MMF coupling scheme described by Grabowski (2004).

2.2. Hyperviscosity

We now proceed to outline the first method envisioned to control MMF stratocumulus entrainment in HR configurations. Models like SAM use oscillatory centered difference numerical schemes (Wicker & Skamarock, 2002) for momentum advection and upstream biased discretizations of scalars with SGS closures have relatively weaker performance than other numerical formulations in an LES case study based on the first research flight (RF01) of the second Dynamics and Chemistry of Marine Stratocumulus (DYCOMS-II) field campaign (Pressel et al., 2017). Wyant et al. (2018) find that in 3D LES simulations with a horizontal resolution of 35 m and vertical grid spacing as fine as 5 m, a hyperdiffusion term helps to increase LWP by numerically damping small-scale eddies and reducing entrainment and entrainment efficiency. We test this method in HR's 2D CRM arrays by applying a hyperdiffusive term (Wyant et al., 2018) to the momentum equation inside the CRM.

The fourth-order hyperdiffusivity can be written as

$$\partial_t \vec{u} = -k\nabla_h^4 \vec{u}, \tag{1}$$

where $k = \Delta x^4/(16\tau)$ is the effective diffusivity and ∇_h^4 operator applies along the horizontal (x) direction of our 2D CRM using the fourth derivative central finite difference with second-order accuracy. Compared to Laplacian diffusivity ∇^2, hyperdiffusivity can more selectively damp the smallest-scale structures confined in smaller wavelength ranges, with little impact on larger scales (Maron et al., 2008). This value of k damps oscillations with Nyquist wavelength on a time scale of τ, which has a default value of 30 s in our simulations.

It is important to note that in LR configurations with $\Delta x = 1{,}200$ m and a Nyquist wavelength of 2,400 m, such hyperviscosity should be expected to be counterproductive, given that LR low clouds rely on under-resolved grid-scale "eddies" to deliver moisture from the surface; in this context, hyperviscosity should be expected to shut down low cloud formation unhelpfully, something we have confirmed (not shown). But in our HR configurations with $\Delta x = 200$ m the use of a filter like Equation 1 is better posed given that the cloud-forming boundary layer eddies occupy multiple horizontal grid columns. Put another way, only as MMFs have exited their infancy to allow sub-km horizontal resolution, has CRM-scale hyperviscosity become an interesting consideration.

19422466, 2024, 3, Downloaded from https://agupubs.onlinelibrary.wiley.com/doi/10.1029/2023MS003632 by University Of Washington, Wiley Online Library on [25/09/2024]. See the Terms and Conditions (https://onlinelibrary.wiley.com/terms-and-conditions) on Wiley Online Library for rules of use; OA articles are governed by the applicable Creative Commons License

2.3. Sedimentation

Our second method to control entrainment efficiency considers a slight modification of HR's simple microphysics. In the one-moment microphysics scheme used in our simulations, condensation occurs when the water vapor amount exceeds saturation, with the excess above saturation converted to liquid, ice, or a mixture of the two depending on temperature. While precipitating liquid and ice (rain, snow, and graupel) sediment as described in M. F. Khairoutdinov and Randall (2003) and Heymsfield (2003), cloud liquid droplets did not sediment in this scheme. Such droplets do sediment in reality and the inclusion of sedimentation in numerical models leads to liquid water retention and increased in-cloud liquid water content (Bretherton et al., 2007). Here, we follow Yau and Rogers (1996) and define the precipitation flux of cloud liquid due to sedimentation as

$$P = c\left[3/\left(4\pi\rho_l N_d\right)\right]^{2/3}\left(\rho q_c\right)^{5/3}\exp\left(5ln^2\sigma_g\right), \tag{2}$$

where ρ is the air density of air, ρ_l the water density, N_d the cloud droplet number concentration, q_c the cloud liquid water mixing ratio, σ_g the geometric standard deviation of the (lognormal) cloud droplet size distribution, and $c = 1.19 \times 10^8$ m^{-1}s^{-1}. The cloud droplet number concentration is prescribed as a constant 70 cm^{-3} over ocean and 140 cm^{-3} over land. A larger value of σ_g corresponds to a broader size distribution and a faster terminal velocity for larger size droplets. Geoffroy et al. (2010) provide estimates of σ_g based on two marine field campaigns, with a central estimate of 1.34 and a parameterization of $sigma_g$ with values ranging from 1.2 to 1.5 for liquid water contents ranging from 0.01 to 2 g m^{-3}. Below, experiments with fixed values of $\sigma_g = 1.2$ and 1.5 are used to characterize the impact of sedimentation in HR MMF.

The cloud optical depth is closely related to the cloud fraction, effective cloud droplet radius, and the in-cloud liquid/ice water content. Following the previous implementation of the single-moment microphysics, fixed values of cloud effective radius for land and ocean are used for all simulations. Only cloud fraction and liquid/ice water content affect cloud optical properties. As we will see, incorporating these effects of sedimentation will reduce entrainment efficiency by drawing liquid down from the inversion zone, especially for larger values of σ_g.

2.4. Experimental Design

By default, E3SM-MMF uses a 60 level vertical grid (L60), which is coarser than the default 72 level grid (L72) used by E3SM. The L72 grid was implicated as the cause of intermittent numerical instability in E3SM-MMF due to very thin layers near the surface, which is often around 20 m thick in the lowest layer. Instead of addressing this by reducing the time step the L60 grid was designed to avoid instability with an approximate thickness of 100 m in the lowest level. Alternatively, the simulations presented here utilize a 125 level grid (L125) that is designed to concentrate refinement roughly between 500 and 1,800 m to improve the representation of sharp temperature inversions needed to represent marine stratocumlus clouds. A smaller CRM time step is used to avoid any numerical issues. Thus, the configuration referred to as "LR" in this study is not the classical cloud SP that uses both coarse vertical and horizontal resolution; rather it can be compared to the "C32-L125-250m" MMF grid configuration of Parishani et al. (2017). According to Bretherton et al. (1999), this vertical grid spacing is not sufficient to resolve entrainment but reflects a pragmatic choice that is computationally affordable in the E3SM-MMF and is intentionally consistent with Parishani et al. (2017).

In Sections 3.1 and 3.3, a computationally efficient configuration will be exploited for hindcast experiments by using a relatively coarse ne16pg2 global grid with 6,144 columns for physics calculations (approximately 2.8° grid spacing). These simulations use a 10 min GCM physics time step. To ensure computational efficiency, the radiation calculations were constrained to 16 columns. This means that radiative heating was computed based on time and spatial averages, considering evenly grouped CRM columns within each GCM column. Each simulation was run for 15 days starting from an initial condition derived from European Centre for Medium-Range Weather Forecasts (ECMWF) Reanalysis (ERA5) atmospheric data (Hersbach et al., 2020) and National Oceanic and Atmospheric Administration (NOAA) sea surface temperature and sea ice data. All hindcast simulations are initialized from 1 October 2008. In our LR hindcast configuration, the embedded CRM has 32 columns with a horizontal grid spacing of 1,200 m (38.4 km extent) and a 5 s CRM time step (see Table 1). Our HR hindcast configuration we use 64 columns with a horizontal grid spacing of 200 m (12.8 km extent) and a 0.5 s CRM time step.

19422466, 2024, 3, Downloaded from https://agupubs.onlinelibrary.wiley.com/doi/10.1029/2023MS003632 by University Of Washington, Wiley Online Library on [25/09/2024]. See the Terms and Conditions (https://onlinelibrary.wiley.com/terms-and-conditions) on Wiley Online Library for rules of use; OA articles are governed by the applicable Creative Commons License

Table 1
A Summary of the Simulations Performed in This Study

Simulation ID	Levels	N	dx (m)	Extent (km)	dt (s)	τ (s)	σ_g
LR	125	32	1,200	38.4	5	–	–
HR	125	64	200	12.8	0.5	–	–
HRh	125	64	200	12.8	0.5	30	–
HRh15	125	64	200	12.8	0.5	15	–
HRs15	125	64	200	12.8	0.5	–	1.5
HRhs12	125	64	200	12.8	0.5	30	1.2
HRhs15	125	64	200	12.8	0.5	30	1.5

Note. N = number of CRM columns; dx = CRM horizontal resolution; τ = damping time scale; dt = CRM time step; σ_g = the logarithmic width of the droplet size distribution, for the simulations that included sedimentation effects.

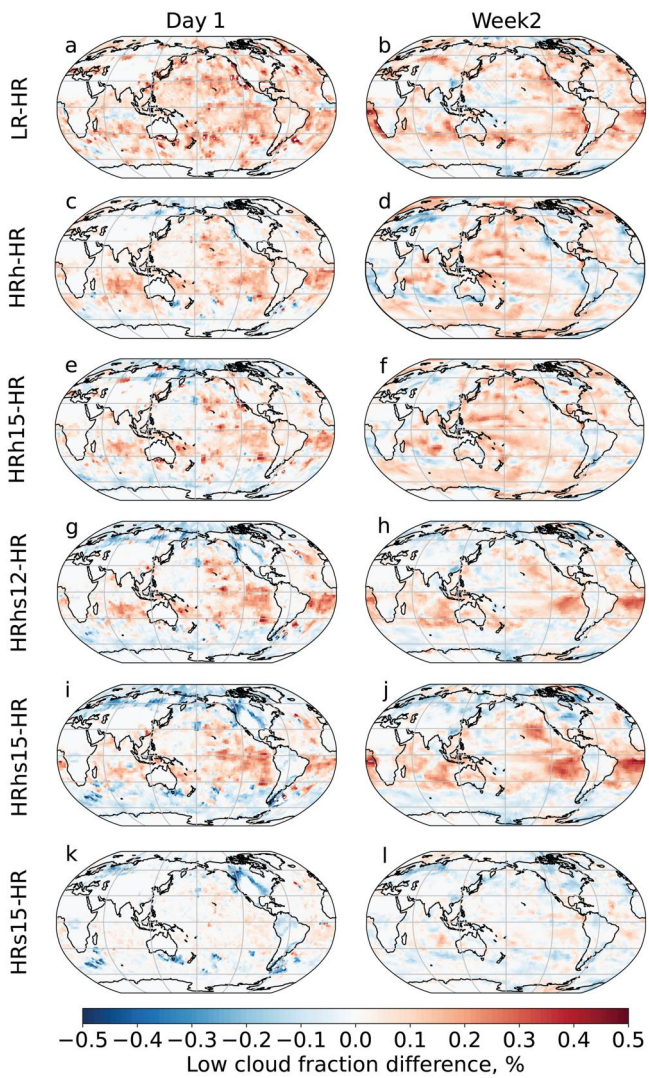

Figure 1. Low cloud fraction differences based on the first day average (left) and 2-week averaged (right) between (a, b) LR and HR (c, d) HRh and HR, (e, f) HRh15 and HR, (g, h) HRhs12 and HR, (i, j) HRhs15 and HR, and (k, l) HRs15 and HR.

The first two hindcast experiments are used to compare the LR and HR configurations (first two rows of Table 1). The rest of the hindcasts are based on the HR configuration and perturb the magnitude of τ in Equation 1 and σ_g in Equation 2. In HRh, we add hyperdiffusion, with $\tau = 30$ s. In HRh15, we test the model sensitivity to the damping time scale with $\tau = 15$ s. Halving τ doubles the magnitude of k in Equation 1, which intensifies the damping of small-scale turbulent eddies; this will turn out to have some encouraging but insufficient improvements in low cloud amount. The HRhs12 and HRhs15 simulations combine hyperdiffusion (with τ fixed at 30 s) with perturbed cloud drop size distributions using $\sigma_g = 1.2$ and 1.5, respectively. As we will see, it is these latter experiments that produce the most encouraging improvement in the stratocumulus dim biases that have hampered past incarnations of HRh.

In Section 3.4, we explore more computationally abitious simulations using a ne30pg2 global grid with 21,600 physics columns (approximately 1.5° grid spacing). These simulations are similar to the HR configuration described above but with several notable differences in their configuration, specifically a 20 min GCM physics time step, a 2 s CRM time step, 256 CRM columns with a horizontal grid spacing of 200 m (51.2 km domain extent), and four radiative columns. The inclusion of hyperdiffusion and sedimentation terms leads to an insignificant impact on the model's overall performance. Table A1 summarizes the computational costs for High Resolution (HR) and Low Resolution (LR) using the ne16pg2 global grid, and for HR both with and without the MMF on the ne30pg2 global grid. Another important difference of these runs is that they utilize schemes for convective momentum transport (Tulich, 2015; Yang et al., 2022) and CRM variance transport (W. Hannah & Pressel, 2022), which have recently been shown to improve various aspects of E3SM-MMF. Each tuning experiment was run for 6 months, from January to June, using seasonally varying climatological conditions based on the years 2005–2014. This ambitious ensemble was made possible by ongoing development to enhance the throughput of E3SM-MMF, which includes code refactoring to leverage GPU hardware acceleration on the Oak Ridge Leadership Computing Facility (OLCF) Summit machine (Norman et al., 2019).

3. Results

3.1. General Features of the Simulation Based on Global Hindcast Results

Because the HR configuration has been identified as suffering from a deficit of low cloud in stratocumulus regions (by as much as 20% in the Sc covered ocean), we simulate 2 weeks hindcasts from October 2008 with the model configurations in Table 1 and seek those configurations that produce sustained more low cloud relative to HR. Figure 1 shows the change in low cloud fraction relative to HR for each model configuration, with results from both the first day and the second week of the simulations used to identify the initial and longer-term responses. As in Parishani et al. (2017), the LR configuration produces increased cloud cover relative to HR, with widespread increases that are not focused in the stratocumulus regions (Figures 1a and 1b). The first encouraging result is that selectively damping small size eddies can retain more subtropical stratucumulus clouds during the first simulated day than HR (geographic patterns in Figures 1c and 1e), but unfortunately that improvement is transient so that this initial effect is not sustained over a 2-week average (Figures 1d and 1f). While enabling sedimentation of cloud

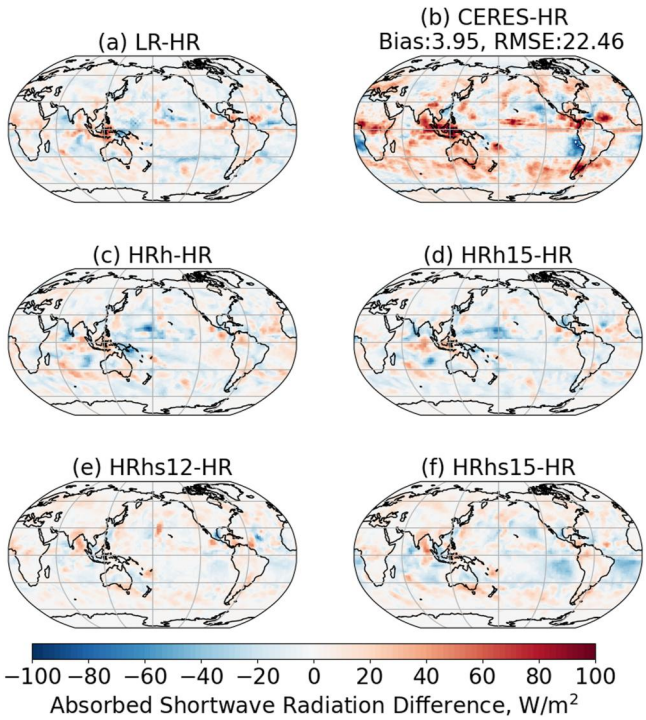

Figure 2. Averaged absorbed shortwave radiation (ASR) differences between (a) LR and HR, (b) CERES and HR, (c) HRh and HR, (d) HRh15 and HR, (e) HRhs12 and HR, and (f) HRhs15 and HR.

droplets provides modest (~0.1%) increases in low cloud in some stratocumulus regions (Figures 1k and 1l), *combining* sedimentation with hyperviscosity leads to an even stronger initial stratocumulus cloud increase (Figures 1g and 1i) that is sustained on longer timescales (Figures 1h and 1j), suggesting a viable path to improve HR's climatological stratocumulus bias. Increasing the droplet size broadness parameter amplifies this effect (Figure 1j).

If one estimated the low cloud change with the combined effects of hyperviscosity and sedimentation in HRhs15 (Figure 1j) as the sum of their individual impacts in HRh and HRs15 (Figures 1d and 1l), the estimate differs greatly from the result in HRhs15 in both its magnitude and in the regional distribution of cloud changes. This nonlinear response in HRhs15 concentrates low cloud increases in the stratocumulus regions, suggesting the synergistic interactions of hyperviscosity and cloud droplet sedimentation lead to more persistent stratocumulus clouds. We believe that these clouds are sustained by more realistic turbulent circulations within the marine boundary layer and will explore this further in Section 3.3.

We next examine whether these cloud fraction increases are radiatively significant relative to the shortwave stratocumulus dim bias of concern. Based on the 2-week averages, Figure 2b first calibrates its structure and magnitude relative to CERES data in our simulations: Note the collection of negative absorbed shortwave radiation (ASR) anomalies over the Sc regions makes a large contribution to the RMSE. Unlike other regional details of the ASR biases that are difficult to disentangle from internal variability in a 15-day sample, the consistent ASR bias over both of the subregions of most subtropical Sc during October (off the western coasts of Namibia and Peru) indicates a robust climatological signal. Despite using a different dynamical core and modeling framework from Parishani et al. (2017), this baseline ASR bias is similar to their C32-L125-250m simulation (their Figure 4b) indicating some stable signals across different MMF implementations.

We now look at change in ASR from this baseline for the simulations with hyperviscosity and sedimentation (Figures 2c–2f). Consistent with its effects on cloud fraction, when hyperviscosity is used in isolation (both HRh and HRh15; Figures 2c and 2d) there is no reduction in the dim bias over Sc regions; rather, the dim bias becomes slightly more pronounced in those simulations. When both effects are combined, cloud induced brightening occurs throughout the stratocumulus regions (relative to HR), except in the near-coastal environment, acting encouragingly in the same direction as the baseline anomalies (negative ASR anomalies off the west coasts of the Namibia, Peru, and Western Australia in Figure 2f). This reduced ASR dim bias corresponds well with the locations of low cloud fraction increase (Figures 1h and 1j). None of the four model perturbations introduce notable outgoing longwave radiation (OLR) differences compared to HR based on the 15-day means (Figure B1).

We now hone in on a strategic subregion of the Southern Hemisphere subtropical Sc latitudes (highlighted in Figure 3a). Inter-model differences of meridionally and time average properties along this zonal transect are shown in Figure 4. The strongest and most interesting changes relative to HR occur when hyperviscosity and sedimentation are combined in HRhs15, producing encouraging Sc brightening that is emphasized in the thick, dark red line. The thick black line serves as a reference, representing the comparison between CERES data and the baseline HR simulation. Closeness to this line—as begins to occur in the eastern parts of the Peruvian (gray) and Namibian (blue) regions, indicates a reduced bias. To orient, the shaded regions (Figure 4) delineate the three Sc zonal subregions highlighted in Figure 3a: off the west coasts of Australia (orange shading), Peru (gray shading), and Namibia (blue shading); in these regions, HRhs15 produced time-mean cloud brightening relative to HR on the order of 20–35 W/m^2. The other panels show that in these same regions HRhs15 also produce 5%–13% more low cloud (Figure 4c) and 0.03–0.05 kg/

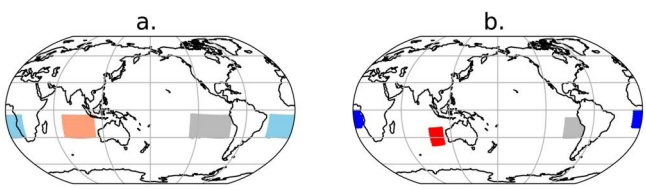

Figure 3. The map of (a) highlighted regions used in Figure 4 and (b) the selected regions to construct height-time plots over Peruvian (gray), West Australian (red), and Namibian (blue).

19422466, 2024, 3, Downloaded from https://agupubs.onlinelibrary.wiley.com/doi/10.1029/2023MS003632 by University Of Washington, Wiley Online Library on [25/09/2024]. See the Terms and Conditions (https://onlinelibrary.wiley.com/terms-and-conditions) on Wiley Online Library for rules of use; OA articles are governed by the applicable Creative Commons License

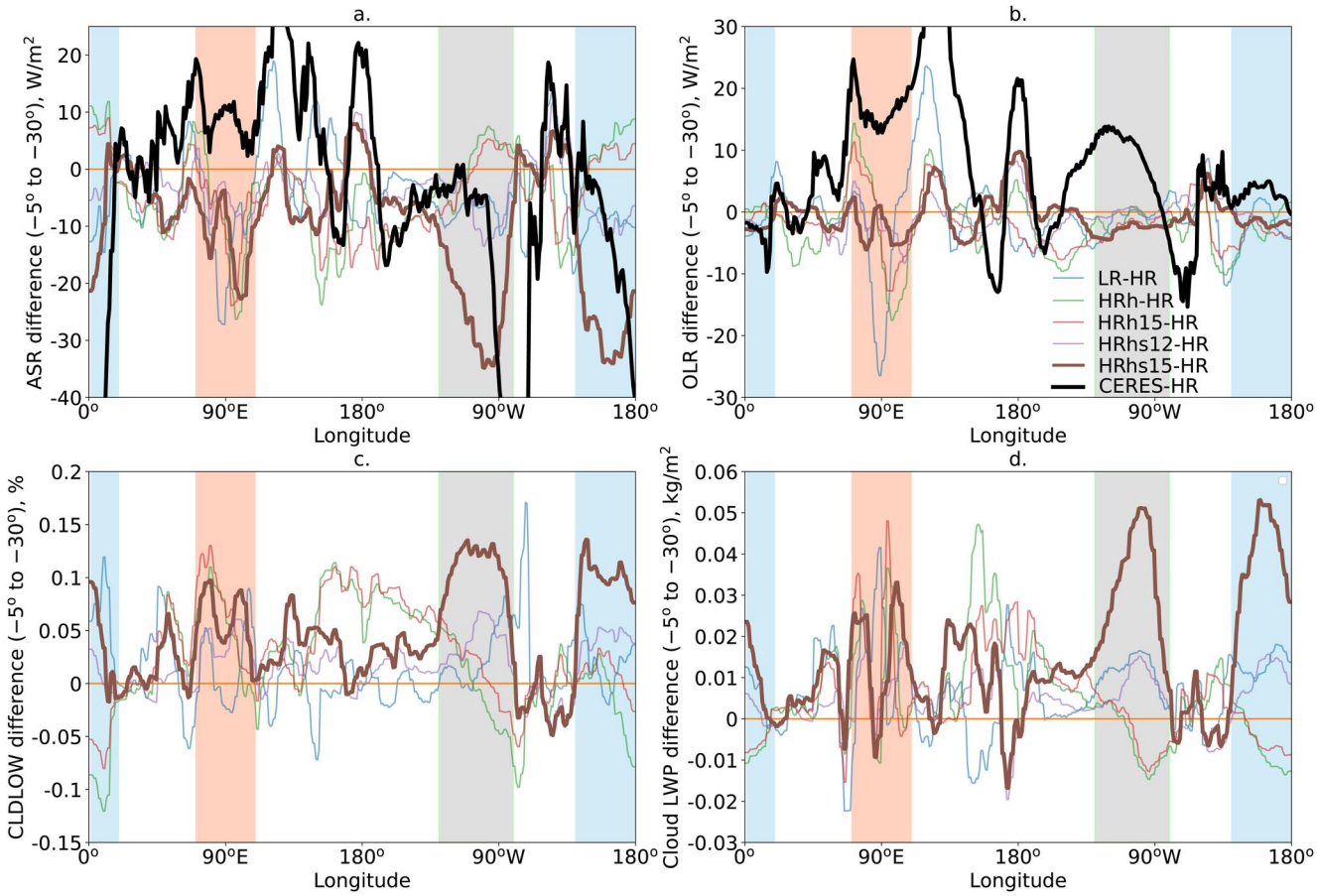

Figure 4. A comparison of (a) the meridional mean absorbed shortwave radiation (ASR) (b) outgoing longwave radiation (OLR), (c) low cloud fraction, and (d) cloud liquid water path (LWP) differences between LR and HR, HRh and HR, HR15 and HR, HRhs12 and HR, HRhs15 and HR, and CERES and HR. The three Sc regions, namely the west coast of Australia, Peru, and Namibia, are represented by the orange, gray, and blue shadings from left to right, respectively.

m^2 larger cloud liquid water paths (Figure 4d). When hyperviscosity is used in isolation (HRh and HRh15), cloud brightening occurs over the Australian Sc deck relative to HR but the dim bias is worsened over the Peruvian and Namibian Sc decks; that is, the effect is not systematic across Sc regimes. Likewise, HRh and HRh15 have either roughly no change or reduced cloud amount relative to HR and liquid water path for the two regions where the dim bias worsens.

In summary, we find robust reductions in the 2-week-mean HR dim bias over the Sc regions in HRhs15 which occur due to increased cloud amount and liquid water path. Changes seem to be due mainly to the synergistic effects of sedimentation and hyperviscosity, as their combined effect is much larger than when either is used in isolation.

3.2. Analysis of Peruvian Stratocumulus Region

This section focuses on the Peruvian Sc region to examine further details of the unsteady evolution of boundary layer vertical structure and the associated changes in low clouds. This region, lying off the west coast of South America over the ocean (gray area in Figure 3b), is one of the most persistent Sc decks (Bretherton & Wyant, 1997) and poorly simulated in models (Konsta et al., 2022).

Figure 5 shows the time-height evolution of CRM-scale vertical velocity variance (shading), a good proxy of low-level turbulent mixing, revealing its co-evolution with cloud fraction (black contours). Both quantities are averaged over the Peruvian Sc region (Figure 3b), as is the time series of liquid water path shown

19422466, 2024, 3, Downloaded from https://agupubs.onlinelibrary.wiley.com/doi/10.1029/2023MS003632 by University Of Washington, Wiley Online Library on [25/09/2024]. See the Terms and Conditions (https://onlinelibrary.wiley.com/terms-and-conditions) on Wiley Online Library for rules of use; OA articles are governed by the applicable Creative Commons License

19422466, 2024, 3, Downloaded from https://agupubs.onlinelibrary.wiley.com/doi/10.1029/2023MS003632 by University Of Washington, Wiley Online Library on [25/09/2024]. See the Terms and Conditions (https://onlinelibrary.wiley.com/terms-and-conditions) on Wiley Online Library for rules of use; OA articles are governed by the applicable Creative Commons License

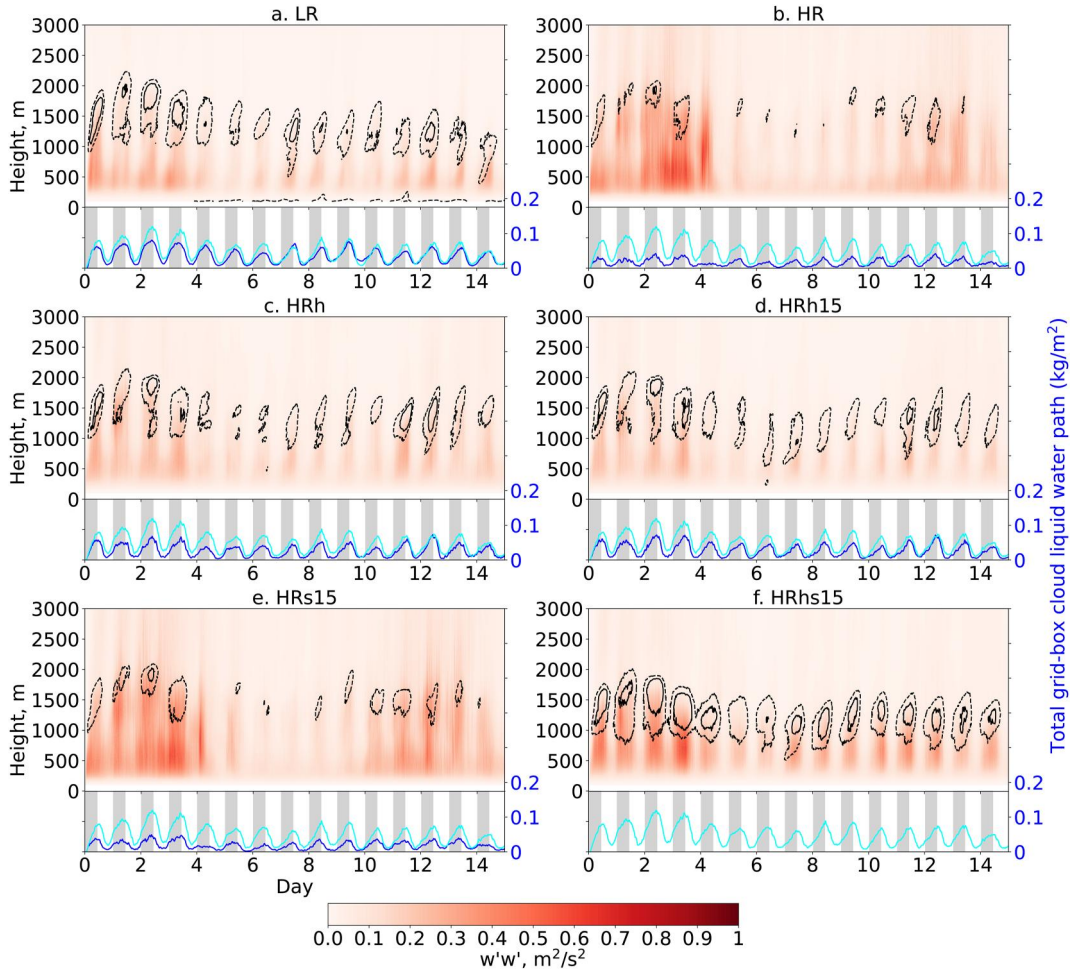

Figure 5. Height time evolution of vertical velocity variance ($\overline{w'w'}$, in units of m^2/s^2) in Peruvian averaged over 15 days starting from 1 October 2008. (a) LR, (b) HR, (c) HRh, (d) HRh15, (d) HRhs12, (f) HRhs15. The blue lines represents the total grid-box liquid water path and cyan line represents HRhs15 for all panels as a reference. Gray shaded time intervals represent nighttime. Black contours are showing the 10% (black dashed line) and 20% (black solid line) cloud fraction.

below each contour plot. The cyan line benchmarks the liquid water path in HRhs15, the simulation that resulted in the most liquid. Strong diurnal cycles are apparent in all simulations, with strong turbulent mixing occurring during local nighttime, as expected (Hignett, 1991). Compared to LR, which uses embedded CRMs that are larger and have a much coarser horizontal resolution, the baseline HR (Figure 5b) produces a larger magnitude of $\overline{w'w'}$ which also extends to a higher altitude, at least during the first few simulated days. These signals and differences between HR and LR are consistent with Parishani et al. (2017), including the inability of HR to sustain low clouds beyond day 4, consistent with its dim bias. Interestingly, in HR some nontrivial $\overline{w'w'}$ is found above the cloud layer, whereas in LR, above-cloud $\overline{w'w'}$ is near-zero. The $\overline{w'w'}$ vertical structure for HR simulation appears to have two modes during the first 2 days of simulation, with one mode near the surface and the other mode closer to the cloud layer, suggesting decoupling. On the other hand, LR only shows one local maximum $\overline{w'w'}$ in the sub-cloud layer with a much weaker magnitude. This local maximum $\overline{w'w'}$ occurs near the surface during daytime and halfway between the surface and cloud level during the nighttime. Although LR does not suffer from a particularly strong over-entrainment bias (Parishani et al., 2017), the cloud layer is supported rather unrealistically by a weak $\overline{w'w'}$ maximum (Heinze et al., 2015; Hignett, 1991; Mechem et al., 2012).

HR has a much smaller cloud fraction and LWP than the other simulations (Figure 5b vs. others), and several symptoms implicate too much entrainment as a key cause. For instance, HR has a much warmer sub-cloud layer

19422466, 2024, 3, Downloaded from https://agupubs.onlinelibrary.wiley.com/doi/10.1029/2023MS003632 by University Of Washington, Wiley Online Library on [25/09/2024]. See the Terms and Conditions (https://onlinelibrary.wiley.com/terms-and-conditions) on Wiley Online Library for rules of use; OA articles are governed by the applicable Creative Commons License

temperature (Figure B2) and this is systematic across Sc regions (Figures B3 and B4). The warming cannot readily be explained by a difference in surface fluxes, given that HR's surface heat fluxes are roughly identical (Figure B2) to the other HR configurations, especially during the first 5 days. We view HR's warm sub-cloud layer as a symptom of over-entrainment of warm overlying free-tropospheric air: As a result of enhanced turbulence through and above the cloud layer in HR, upward water transport is unable to sustain the cloud against entrainment-driven warming and drying. In summary, we suspect that strong $\overline{w'w'}$ near cloud top leads to over-entrainment, and that this is the main cause of the dim bias over Sc regions in the baseline HR simulation.

We now analyze our attempts to reduce over-entrainment, beginning with applying hyperviscosity in isolation. We expect this to directly reduce $\overline{w'w'}$ associated with small eddies regardless of whether they were associated with moist processes. Indeed, above the cloud layer, adding the hyperviscosity term with $\tau = 30$, 15 s helps to reduce the above-cloud magnitude of $\overline{w'w'}$ (Figures 5c and 5d) compared with HR (Figure 5b). Encouragingly, the low cloud fraction also increases throughout the simulation. But the additional low cloud is only recovered at night, which explains why hyperviscosity alone is not able to alleviate the shortwave dim bias. Reducing τ from 30 to 15 s (HRh15) helps to further reduce $\overline{w'w'}$ (Figure 5d), but has minimal effects on low cloud fraction beyond those of HRh; indeed this is why we use $\tau = 30$ s as our default value for the hyperviscosity term. As pointed out earlier, despite being encouraging, the effects of hyperviscosity alone are not enough to fully address the over-entrainment problem that causes HR to be unable to sustain enough low cloud. One signature of turbulence driven by healthy amounts of cloud top radiative cooling is an elevated peak in $\overline{w'w'}$ away from the surface; note that this is too weak in HRh.

We now examine the impact of additionally including cloud droplet sedimentation (Figure 5f). Removing cloud water away from the cloud top via sedimentation results in a *larger* $\overline{w'w'}$ and a promising improvement in overall low cloud fraction. As suggested by Bretherton et al. (2007), this is driven by a reduction of the entrainment efficiency due to reduced liquid in the cloud-top entrainment zone. Reassuringly, the strongest $\overline{w'w'}$ is now found well above the surface and in the upper half of the boundary layer, consistent with cloud-top buoyancy production being the primary driver of convection, especially during the nighttime as observed. Thick clouds persist beyond the first week of the simulation as a result of the reduced consumption of cloud liquid by entrainment. Again, these effects only occur in conjunction with hyperviscosity. Incorporating sedimentation on its own results in a reduced cloud fraction and a weaker $\overline{w'w'}$ (Figure 5e).

Differences in inversion height are subtle to detect visually, but Table 2 summarizes median properties from cloudy grid points (nonzero liquid water) in each simulation (averaged between days 2 and 15). The inversion height (z_i) shown in Table 2 generally agrees with what was observed during the Ocean–Cloud–Atmosphere–Land Study Regional Experiment (VOCALS-REx) at Point Alpha in October and November 2008 off the coast of South America, which varied between 996 and 1,450 m (Dodson & Small Griswold, 2021). We note that HRhs15 has the smallest difference between the cloud top height and the inversion height while HR has the largest, which we connect to inversion strength in the next section.

Table 2 also quantifies the decoupling that was discussed subjectively in Figure 5. We estimated the decoupling parameters for water vapor mixing ratio (q) as $\alpha_q = \frac{q_{cld} - q_{ml}}{q_{inv} - q_{ml}}$ (Park et al., 2004). Subscripts *cld*, *inv*, and *ml* refer to mean values between the cloud base and top, between the surface and cloud base, and at the inversion height respectively. A decoupling parameter close to zero indicates a well-mixed boundary layer. Previous observations suggest that the boundary layer is decoupled when the parameter exceeds about 0.30 (Albrecht et al., 1995). HR produces the highest values for α_q during the nighttime. There is much less contrast in daytime than nocturnal decoupling in HRhs15 compared with other configurations. A vertically decoupled thermodynamic structure produces cloud bases well above the LCL (Miller et al., 1998); indeed the cloud base is 103 m (81 m) above the LCL for HR during the daytime (nighttime), while 93 m (70 m) for HRhs15. In the baseline HR, more decoupling can be viewed as a symptom of over-entrainment that is likely to cause less Sc during the daytime in that reduced moisture supply at cloud base cannot overcome the dry air entrainment from cloud top. HRhs15 corresponds to a lower entrainment rate (w_e) during the daytime than HR and HRh. HRhs15 also corresponds to the largest magnitude of shortwave cloud effects (SWCRE) due to a larger cloud fraction.

19422466, 2024, 3, Downloaded from https://agupubs.onlinelibrary.wiley.com/doi/10.1029/2023MS003632 by University Of Washington, Wiley Online Library on [25/09/2024]. See the Terms and Conditions (https://onlinelibrary.wiley.com/terms-and-conditions) on Wiley Online Library for rules of use; OA articles are governed by the applicable Creative Commons License

Table 2
Median Values From Day 2 to Day 15 for Selected Variables During Daytime With Nighttime Values in Parenthesis

	LR	HR	HRh	HRhs15
Cloud fraction (%)	44 (73)	27 (46)	31 (63)	49 (73)
LWP (g/m^2)	19 (43)	7 (19)	10 (13)	24 (55)
z_i (m)	1,301 (1,216)	1,414 (1,358)	1,387 (1,298)	1,266 (1,212)
Cloud top (m)	1,212 (1,157)	1,218 (1,283)	1,215 (1,224)	1,195 (1,195)
Cloud base (m)	732 (661)	752 (705)	753 (685)	653 (618)
z_{LCL} (m)	630 (591)	649 (624)	639 (602)	560 (548)
α_q	0.24 (0.22)	0.22 (0.27)	0.22 (0.26)	0.23 (0.24)
w_e (mm/s)	3.6 (3.9)	4.3 (3.8)	4.3 (3.8)	4.0 (3.8)
SWCRE (W/s^2)	59 (−)	23 (−)	32 (−)	71 (−)

Note. This calculation discards 10% of the upper and lower outlier points before estimating the median values. *LWP* = Total grid-box cloud liquid water path; z_{LCL} = Lifting condensation level; z_i = Inversion height; α_θ = decoupling parameters for potential temperature; α_q = Decoupling parameters for water vapor mixing ratio; w_e = Entrainment rate (estimated as the subsidence rate at z = zi, assuming a steady state); *SWCRE* = Shortwave cloud forcing (values are all negative during the daytime).

3.3. Composite Vertical Structure and Turbulent Scale Analysis

We now examine mean daytime (dashed) and nighttime (solid) vertical profiles (Figure 6) from days 2–15 over the Peruvian region. Here, the height, z, is normalized by the inversion height (z_i) to give a nondimensional vertical coordinate, z/z_i.

All configurations show a large diurnal cycle: the daytime cloud liquid water content is about half of its nighttime value. HRhs15 (HR) corresponds to the largest (lowest) cloud liquid water content in both nighttime and daytime

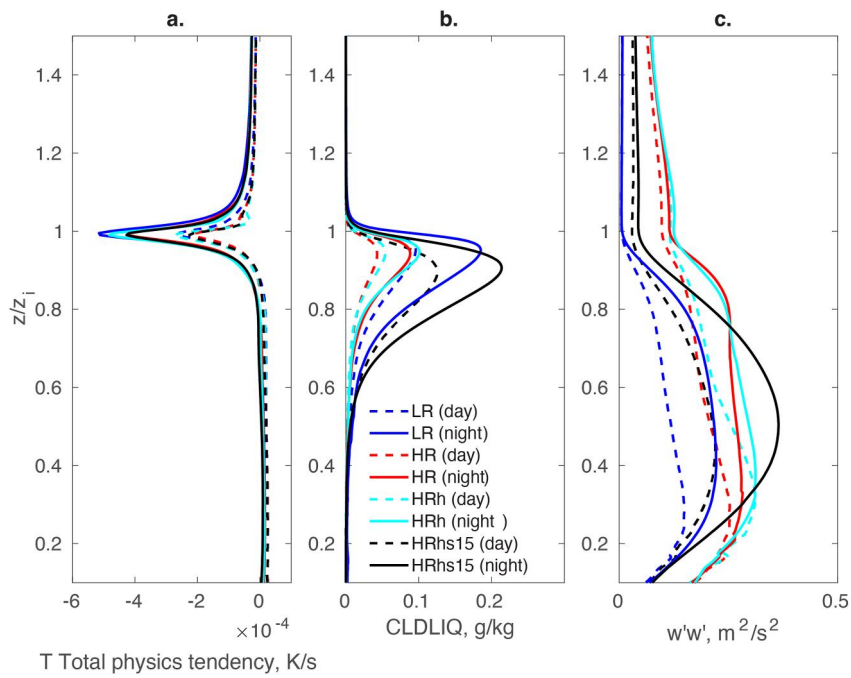

Figure 6. Averaged vertical profiles normalized by z_i from day 2 to day 15 for (a) T total physics tendency (*K/s*), (b) cloud liquid water content (g/kg), and (c) $\overline{w'w'}$ (m^2/s^2). Solid lines represent night time average, while dashed lines represent the day time average.

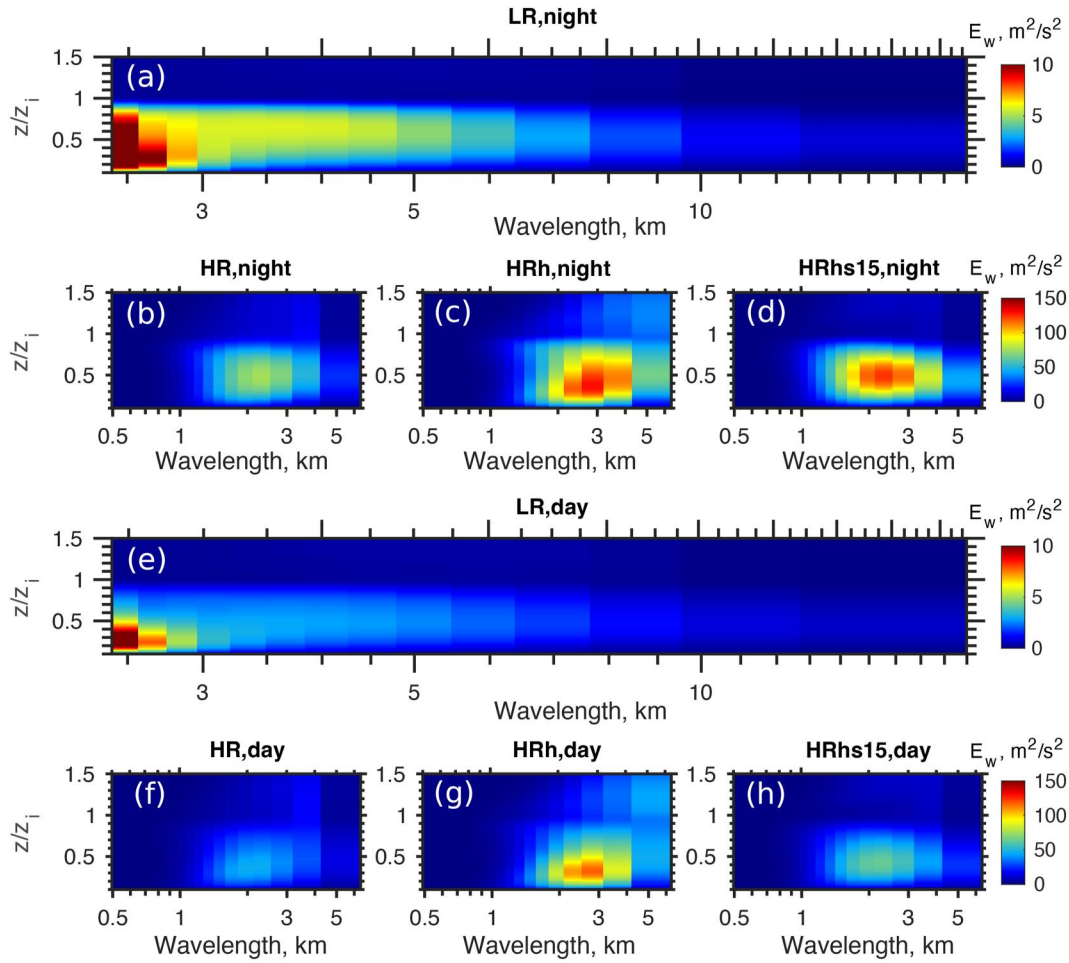

Figure 7. A comparison of vertical profiles of the spectral intensity for nighttime average of (a) LR, (b) HR, (c) HRh, and (d) HRhs15, and daytime average of (e) LR, (f) HR, (g) HRh, and (h) HRhs15.

groups. It is interesting to note that HRhs15 has an even higher daytime cloud liquid water content than nighttime HR; in fact, in the following section we will show that there is too much daytime liquid in HRhs15, motivating compensatory microphysical retuning.

Longwave radiative cooling at the cloud top is regarded as the primary driver of convection in stratocumulus clouds (Lilly, 1968; Moeng et al., 1996; Nicholls, 1989). Note that the peak cloud top radiative cooling that has the largest contribution to the total temperature tendency (Figure 6a) occurs at the cloud top (van Zanten, 2002). Regardless of the large magnitude of $\overline{w'w'}$ (Figure 6c), HRhs15 has slightly lower cloud top radiative cooling compared with LR and HRh (Figure 6a) due to less liquid emissivity near the cloud top. The level corresponding to the highest cloud liquid water content (Figure 6b) is similar for LR, HR, and HRh, but this level is lower and further away from the cloud top for HRhs15 due to sedimentation. While HRhs15 and HR have a similar magnitude of cloud top radiative cooling, this radiative cooling produces a thicker cloud and drives stronger and better coupled vertical motions $\overline{w'w'}$ in HRhs15 than HR due to its weaker entrainment. A smaller magnitude of cloud top radiative cooling for HR during the daytime might also help to explain the warmer sub-cloud layer temperature compared with HRh, especially after day 7 shown in Figure B2a. On the other hand, this warming is less severe compared between HR and HRhs15 near the cloud top.

It is still not clear whether cloud top entrainment is controlled by small eddies or large eddies (Wood, 2012). To more closely examine the eddy spectra in cloudy regions, we perform spectral analysis along the CRM's horizontal dimension looking at the power spectrum of the CRM-scale vertical velocity, separately for daytime and nighttime (Figure 7).

19422466, 2024, 3, Downloaded from https://agupubs.onlinelibrary.wiley.com/doi/10.1029/2023MS003632 by University Of Washington, Wiley Online Library on [25/09/2024]. See the Terms and Conditions (https://onlinelibrary.wiley.com/terms-and-conditions) on Wiley Online Library for rules of use; OA articles are governed by the applicable Creative Commons License

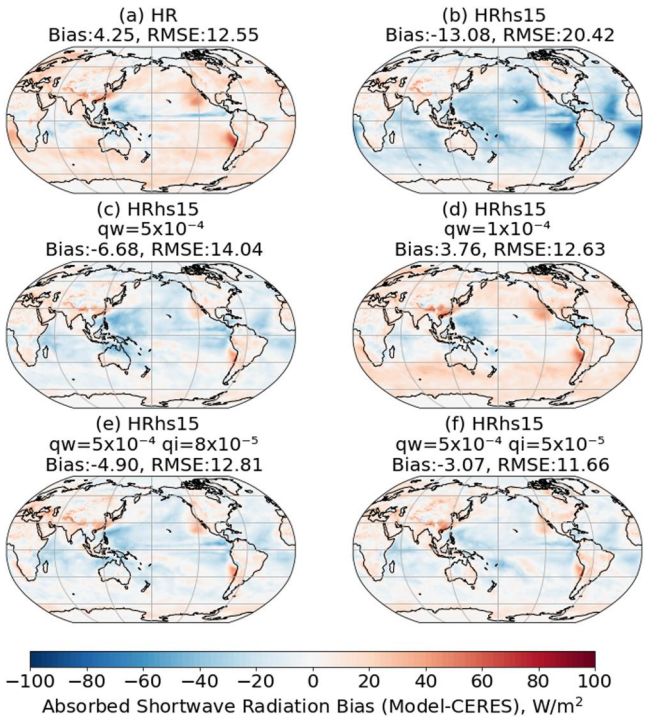

Figure 8. Absorbed shortwave radiation at TOA biases with respect to CERES for the (a) HR, (b) HRhs15 with default configuration, (c) HRhs15 with $q_w = 5 \times 10^{-4}$, (d) HRhs15 with $q_w = 1 \times 10^{-4}$, (e) HRhs15 with $q_w = 5 \times 10^{-4}$ and $q_i = 8 \times 10^{-5}$ (d) HRhs15 with $q_w = 5 \times 10^{-4}$ and $q_w = 5 \times 10^{-5}$.

Compared with HR (Figures 7b and 7f), the spectral intensity distribution for HRhs15 (rightmost column) is clearly confined within the stable boundary layer (STBL) with a single peak near $0.5z_i$.The magnitude of this peak is larger during the nighttime since nighttime has a larger LWP. In HRh, the spectral intensity distribution peaks at toward larger wavelengths (Figures 7c and 7g). In HRh, the spectral intensity of small eddies (wavelengths close to $2\Delta x = 400$ m) is reduced, while the spectral power above the cloud top is enhanced with the large eddies (wavelengths greater than 2,000 m). HRh has the strongest signals close to the largest wavelength that can be resolved (half of the domain size). LR is able to resolve eddies with horizontal wavelengths of up to 10 km thanks to its larger domain size (Figures 7a and 7e). However, the occurrence of the peak eddy spectral density for the smallest resolvable eddies (2.4 km) indicates eddy variance pile-up on the grid-scale. This implies that cloud-forming eddies, which are constrained by the numerical grid's finest resolved scale, are under-resolved in the low resolution simulation. The HR configurations are more physically plausible representations of sub-cloud turbulence in that a spectral peak exists interior to the resolvable scales. The high resolution of HR permits sub-cloud eddies to occupy multiple horizontal grid columns. We still can see relatively strong eddies (wavelengths around 3,000 m) above the cloud. While HRhs15 may also cut off signals due to limited domain size, its spectral intensity distribution clearly shows a much better range of the resolved signal and STBL structure that is more consistent with observations and expectations from LES.

HRhs15 also corresponds to the weakest above cloud eddies to reduce entrainment. Close to the inversion height (z_i), a stronger stratification tends to reduce the magnitude of E_w and the dominant wavelength corresponding to the maximum E_w. Unlike HRhs15, relatively large vertical velocity fluctuations above the inversion height in HR and HRh corresponds well with a reduce the temperature inversion and, therefore, does not have a significant impact on the wavelength near the cloud top (e.g., Figure 7b). Above z_i, the eddies are much larger than they are below z_i.

3.4. Microphysics Tuning

The previous sections have provided evidence that the addition of hyperviscosity and cloud droplet sedimentation produces encouraging changes in stratocumulus clouds such as more daytime clouds. However, the coarse global mesh, smaller CRM domains and short, 2 weeks duration of the hindcast simulations analyzed above represent notable compromises when compared to standard configurations of E3SM and E3SM-MMF. To address this concern we have conducted a series of 6-month simulations using the ne30pg2 grid and a larger CRM domain (Section 2.4) that is more typical for E3SM experiments. These simulations are a subset of a larger tuning effort that considered several microphysical parameters. Ultimately, we found that autoconversion thresholds for liquid ($q_{cw0} = 1 \times 10^{-3}$ by default) and ice ($q_{ci0} = 1 \times 10^{-4}$ by default) were the most effective parameters for bringing the TOA energy fluxes into a reasonable balance and so that is what we will focus on below. This tuning exercise was partially motivated by the observation that the low-cloud enhancement resulting from the use of hyperviscosity and cloud droplet sedimentation produced a dramatic change in the TOA net shortwave radiative flux (Figure 8b).

Figure 8 shows a comparison of the absorbed shortwave radiation climatological biases from our 10-year simulation compared with satellite observations. The baseline HR and several retunings of the baseline HRhs15 configuration are compared. Unlike HR, the ASR bias for HRhs15 primarily stems from too bright marine clouds, especially over the subtropical Sc regions (Figure 8). Especially strong negative ASR biases are found off the western coasts of Peru, Namibia, Australia, and California. Reducing the liquid autoconversion thresholds increases the ASR (Figures 8b–8d), approximately halving the global mean shortwave

19422466, 2024, 3, Downloaded from https://agupubs.onlinelibrary.wiley.com/doi/10.1029/2023MS003632 by University Of Washington, Wiley Online Library on [25/09/2024]. See the Terms and Conditions (https://onlinelibrary.wiley.com/terms-and-conditions) on Wiley Online Library for rules of use; OA articles are governed by the applicable Creative Commons License

19422466, 2024, 3, Downloaded from https://agupubs.onlinelibrary.wiley.com/doi/10.1029/2023MS003632 by University Of Washington, Wiley Online Library on [25/09/2024]. See the Terms and Conditions (https://onlinelibrary.wiley.com/terms-and-conditions) on Wiley Online Library for rules of use; OA articles are governed by the applicable Creative Commons License

Table 3
The Bias and RMSE in Parenthesis for Ocean and Land

			ASR (W m^{-2})		OLR (W m^{-2})	
	q_{cw0} (kg kg^{-1})	q_{ci0} (kg kg^{-1})	Ocean	Land	Ocean	Land
HR	1×10^{-3}	1×10^{-4}	4.0(9.5)	1.5(4.4)	−8.2(8.6)	−2.0(2.8)
HRhs15	10^{-3}	1×10^{-4}	−19.5(18.6)	−2.1(4.3)	−7.7(8.1)	1.5(3.2)
HRhs15	5×10^{-4}	1×10^{-4}	−10.4(11.3)	−1.1(4.4)	−5.9(7.0)	0.1(3.2)
HRhs15	1×10^{-4}	1×10^{-4}	3.0(9.7)	2.6(4.4)	−3.9(6.2)	−1.1(2.7)
HRhs15	5×10^{-4}	8×10^{-4}	−8.6(10.3)	−0.2(4.1)	−4.8(6.1)	1.3(3.1)
HRhs15	5×10^{-4}	5×10^{-4}	−6.9(8.9)	1.8(4.1)	−2.8(4.7)	2.9(2.8)

bias, and reduces the RMSE. A reduced liquid autoconversion threshold combined with an increased ice autoconversion threshold further helps to ameliorate ASR global mean bias and reduce RMSE (Figures 8e and 8f). The configuration with $q_{cw0} = 5 \times 10^{-4}$ and $q_{ci0} = 5 \times 10^{-5}$ produces the smallest global mean bias and RMSE (Figure 8e). Most of this improvement occurs over the ocean (Table 3). Even with the microphysics retuning, the incorporation of hyperviscosity and sedimentation continues to play a crucial role in reducing the ASR bias particularly over regions covered by stratocumulus clouds (Figure B5).

Microphysical tuning results in weaker changes of OLR than those for ASR (Figure 9). Sedimentation (HRhs15) only slightly increased the global mean OLR (Figures 9a and 9b) from the base HR simulation, which was too opaque in the tropics. This bias is reduced in Figure 9f. Overall, we are able to obtain less than 1 W/m^2 OLR bias.

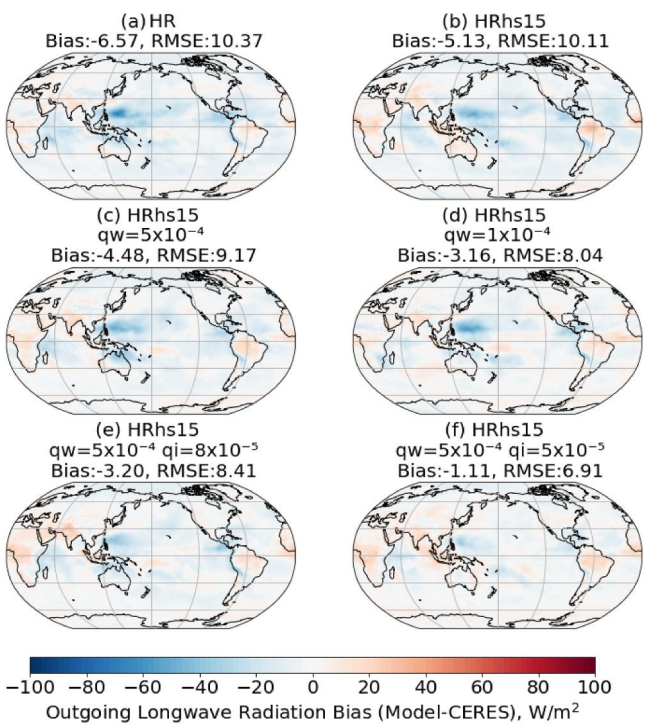

Figure 9. Outgoing longwave radiation at TOA biases with respect to CERES for the (a) HR, (b) HRhs15 with default configuration, (c) HRhs15 with $q_w = 5 \times 10^{-4}$, (d) HRhs15 with $q_w = 1 \times 10^{-4}$, (e) HRhs15 with $q_w = 5 \times 10^{-4}$ and $q_i = 8 \times 10^{-5}$ (d) HRhs15 with $q_w = 5 \times 10^{-4}$ and $q_w = 5 \times 10^{-5}$.

4. Discussion and Conclusions

Compared to other available global modeling tools for studying cloud feedback, today's GPU-accelerated Multiscale Modeling Frameworks configured with High Resolution (HR) interior grids have the capacity to provide a unique combination of global eddy-permitting resolution coverage and multi-decadal throughput that complements other climate simulation technology. In theory HR MMFs should be attractive for low cloud feedback analysis and cloud-aerosol interactions, by making minimal assumptions about the sub-km scale vertical eddy field.

But in practice, this depends on the model's ability to represent present-day climate. For over 5 years since the first experiments with HR MMF, it has been unclear whether a chronic over-entrainment bias preventing realistic amounts of Sc liquid water was surmountable. It has been natural to wonder if the inherent idealizations of MMFs that make them computationally attractive —that is, the limited domain size, dimensionality, moderate (200-m) interior horizontal resolution, lateral periodicity, and associated inability to laterally advect liquid water conservatively—(Jansson et al., 2022; Muller & Held, 2012)—might impose fundamental limitations.

Our results argue otherwise: We suggest MMFs are simply in their infancy and their interior resolved scale has never been sufficiently tuned to succeed in a HR limit. To show this, we investigated the impact of adding hyperviscosity and sedimentation on low cloud formation in a high resolution multi-scale modeling framework (HR) that uses 200-m horizontal, and as fine as 20-m vertical, grid spacing within each of its embedded convection resolving models, configured with bulk one-moment microphysics. As in previous studies, our control HR simulation produced the familiar bias of too few low clouds over regions of subtropical marine stratocumulus (Sc),

19422466, 2024, 3, Downloaded from https://agupubs.onlinelibrary.wiley.com/doi/10.1029/2023MS003632 by University Of Washington, Wiley Online Library on [25/09/2024]. See the Terms and Conditions (https://onlinelibrary.wiley.com/terms-and-conditions) on Wiley Online Library for rules of use; OA articles are governed by the applicable Creative Commons License

resulting in a dim bias compared with satellite observations of shortwave radiation absorbed at top of atmosphere.

We found promising Sc-selective brightening when we combined scale selective damping (hyperviscosity) of grid scale momentum variations with the introduction of cloud droplet sedimentation. The application of hyperviscosity alone, which directly reduces $\overline{w'w'}$, leads to short-lived increases in nocturnal cloud thickness. Simulations with sedimentation alone lead to modest increases in cloud fraction. However, the most encouraging effects occur when the two are applied together, whereupon robust increases in cloud liquid water lead to a reversal of the Sc dim bias, including in multi-week integrations. These nonlinear interactions of these two processes lead to much stronger changes than when they are applied separately. The resulting, larger peak liquid water concentration is shifted downward, away from the cloud-top entrainment zone. In this configuration, dense, locally formed Sc are observed to form in the HR MMF, and the sub-cloud eddy spectrum becomes especially well organized.

In summary, with only these minor, physically motivated re-tunings, the CRMs of a HR MMF can be coerced to create healthy amounts of locally generated stratocumulus liquid, in association with reasonable sub-cloud eddy properties. This is possible despite the assumptions of periodicity, dimensionality (2D) and only 200-m horizontal resolution that makes HRs computationally efficient, which is encouraging. At first, the interventions create too much low cloud, and swap a regional dim bias for a global ocean bright bias—but with encouragingly little horizontal variation across the oceanic cloud regimes, with hope for calibration. Thus, as must occur following any manipulation of a MMF's physical formulation, we performed a compensatory microphysical re-tuning to recover a reasonable top of atmosphere climatology. Despite a limited tuning campaign, the results demonstrate the potential for significantly less severe Sc dim biases, and reduced spatial RMSE of shortwave absorbed radiation across the global ocean. It is logical to expect that with further attention to tuning, even more operationally attractive configurations could be uncovered.

Several limitations of this work are worth mentioning. In our current study, we did not fully explore the contribution of resolved scale advection and subgrid scale diffusion to the reduced entrainment efficiency caused by hyperviscosity. With enhanced outputs including the SGS contribution in SAM, future investigations could evaluate these aspects to gain a deeper understanding of the underlying mechanisms. We speculate a root problem motivating the need to apply hyperviscosity in our simulations may be the numerics of the momentum solver in the embedded CRM (see Section 2.1). Successors to SAM under development by DOE for use in E3SM-MMF, like most modern LES (Eldred, 2021), intentionally use a cell-centered, entropy stable Weighted Essentially Non-Oscillatory (WENO) schemes for the momentum solver, as suggested in the work of Pressel et al. (2017). Another obvious limitation is that the HR here uses a simple one-moment microphysics scheme and diagnostic turbulence scheme. While this is helpful for maximizing throughput at its ambitious grid resolution, it is also outdated. The eventual higher-order microphysics (Morrison & Milbrandt, 2015) that are expected to come online in the E3SM-MMF may suffer less from baseline over-entrainment due to already including a representation of the sedimentation process that we have argued helpfully draws cloud liquid down from the inversion to optimize entrainment efficiency. Perhaps this imminent next generation of HR will have less need for compensatory CRM-scale tuning and less sensitivity to grid spacing to achieve its low cloud potential.

Then again, perhaps not. For now, it is clear that "multi-scale" modeling frameworks seem to merit careful "multi-scale" physics calibration, and that this has largely been overlooked on the interior resolved scale, at least in explorations of MMF at the limit of HRs' grid resolutions. On the one hand, this annoyingly complicates the art of global model tuning. On the other hand, it is good news for the long term potential to study low-cloud feedbacks quasi-explicitly via the HR MMF approach. Despite its idealizations, healthy amounts of present-day Sc cloud can evidently be recovered in an HR MMF, allowing its computational advantages to be brought to bear on questions of cloud feedback. It will be important to determine whether this modifies previous estimates of the HR MMF low cloud feedback to warming (Parishani et al., 2018) from previous generation simulations that have struggled to capture sufficient baseline low cloud.

Appendix A: Tables

Table A1.

Table A1
A Summary of the Computational Cost

HPC system	Simulation ID	GCM resolution	Simulated year per day	Node hour
Frontera (CPU)	LR	ne16pg2	0.04	644
	HR	ne16pg2	0.02	1,289
Summit (V100 GPU)	HR(no MMF)	ne30pg2	23.51	65
	HR	ne30pg2	0.61	2,518

Note. Our ne16pg2 simulations were conducted on the Frontera (High-Performance Computing) HPC system, which has 56 CPUs per node. For the ne30pg2 simulations, we utilized the Summit HPC system. Each MMF simulation used 128 nodes on the Summit GPU cluster, with 6 MPI tasks and 7 OMP threads per node. This represents the state of GPU-accelerated MMF simulation performance on V100-era GPUs.

Appendix B: Figures

Figure B1, Figure B2, Figure B3, Figure B4, and Figure B5.

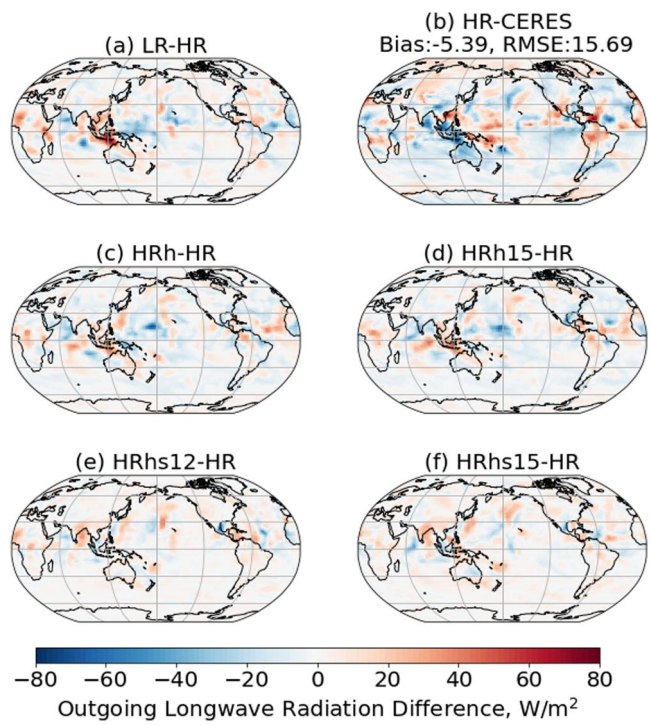

Figure B1. Similar to Figure 2 but for outgoing longwave radiation (OLR) difference.

19422466, 2024, 3, Downloaded from https://agupubs.onlinelibrary.wiley.com/doi/10.1029/2023MS003632 by University Of Washington, Wiley Online Library on [25/09/2024]. See the Terms and Conditions (https://onlinelibrary.wiley.com/terms-and-conditions) on Wiley Online Library for rules of use; OA articles are governed by the applicable Creative Commons License

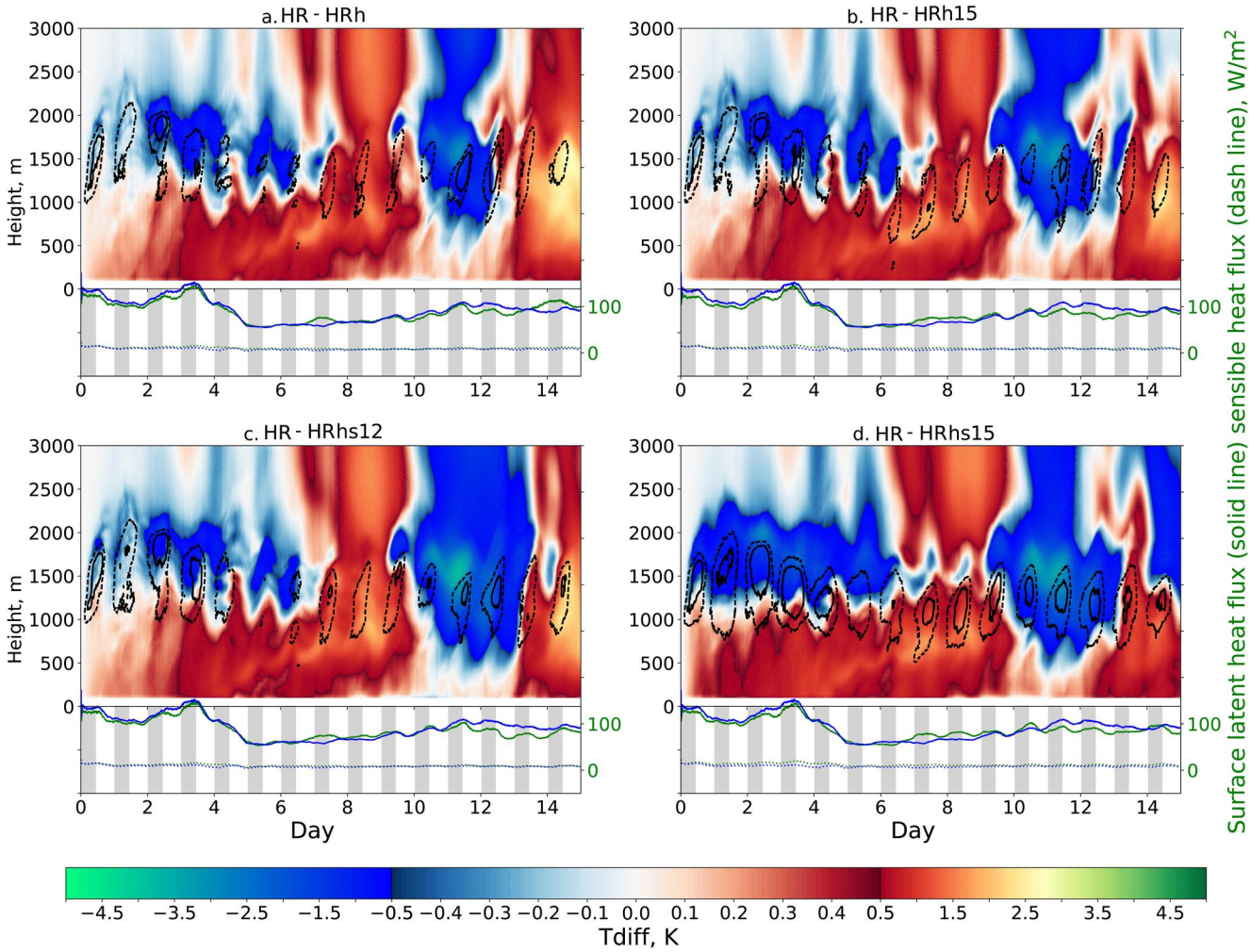

Figure B2. Height time evolution of temperature difference over Peruvian between HR and (a) HRh, and (b) HRh15, (c) HRhs12, and (d) HRhs15. Surface sensible (dashed lines) and latent heat (solid lines) flux are shown by blue lines for HR and green lines for other configurations. Two cloud fraction contour lines for other configurations been subtracted by HR are shown for 0.1 (black dotted line) and 0.2 (black solid line).

19422466, 2024, 3, Downloaded from https://agupubs.onlinelibrary.wiley.com/doi/10.1029/2023MS003632 by University Of Washington, Wiley Online Library on [25/09/2024]. See the Terms and Conditions (https://onlinelibrary.wiley.com/terms-and-conditions) on Wiley Online Library for rules of use; OA articles are governed by the applicable Creative Commons License

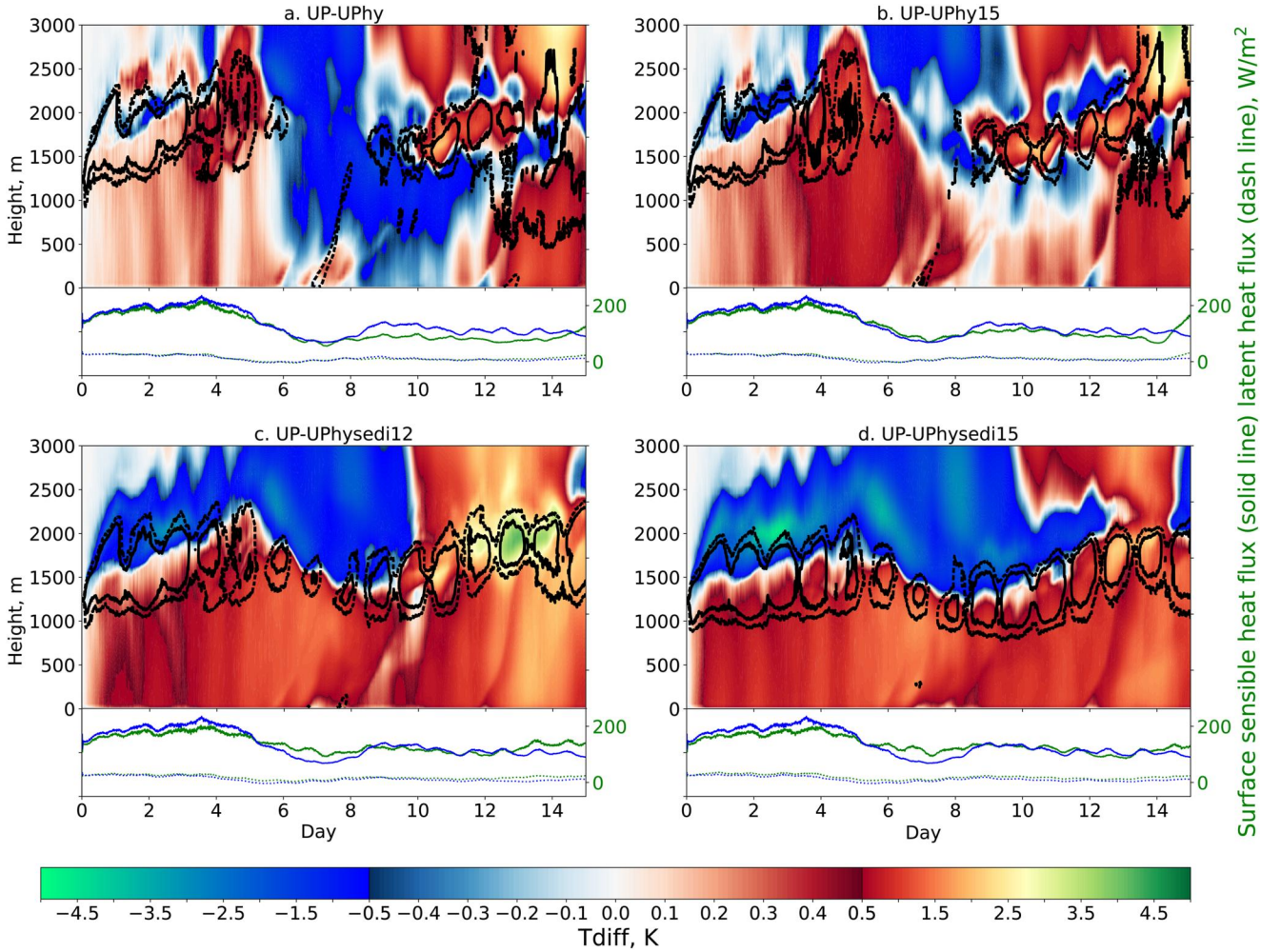

Figure B3. Height time evolution of temperature difference in west coast Australia between HR and (a) HRh, and (b) HRh15, (c) HRhs12, and (d) HRhs15. Surface sensible and latent heat flux are shown by blue solid and dashed lines for HR (blue) and other configurations (green). Two cloud fraction contour lines are 0.1 (black dotted line) and 0.2 (black solid line).

19422466, 2024, 3, Downloaded from https://agupubs.onlinelibrary.wiley.com/doi/10.1029/2023MS003632 by University Of Washington, Wiley Online Library on [25/09/2024]. See the Terms and Conditions (https://onlinelibrary.wiley.com/terms-and-conditions) on Wiley Online Library for rules of use; OA articles are governed by the applicable Creative Commons License

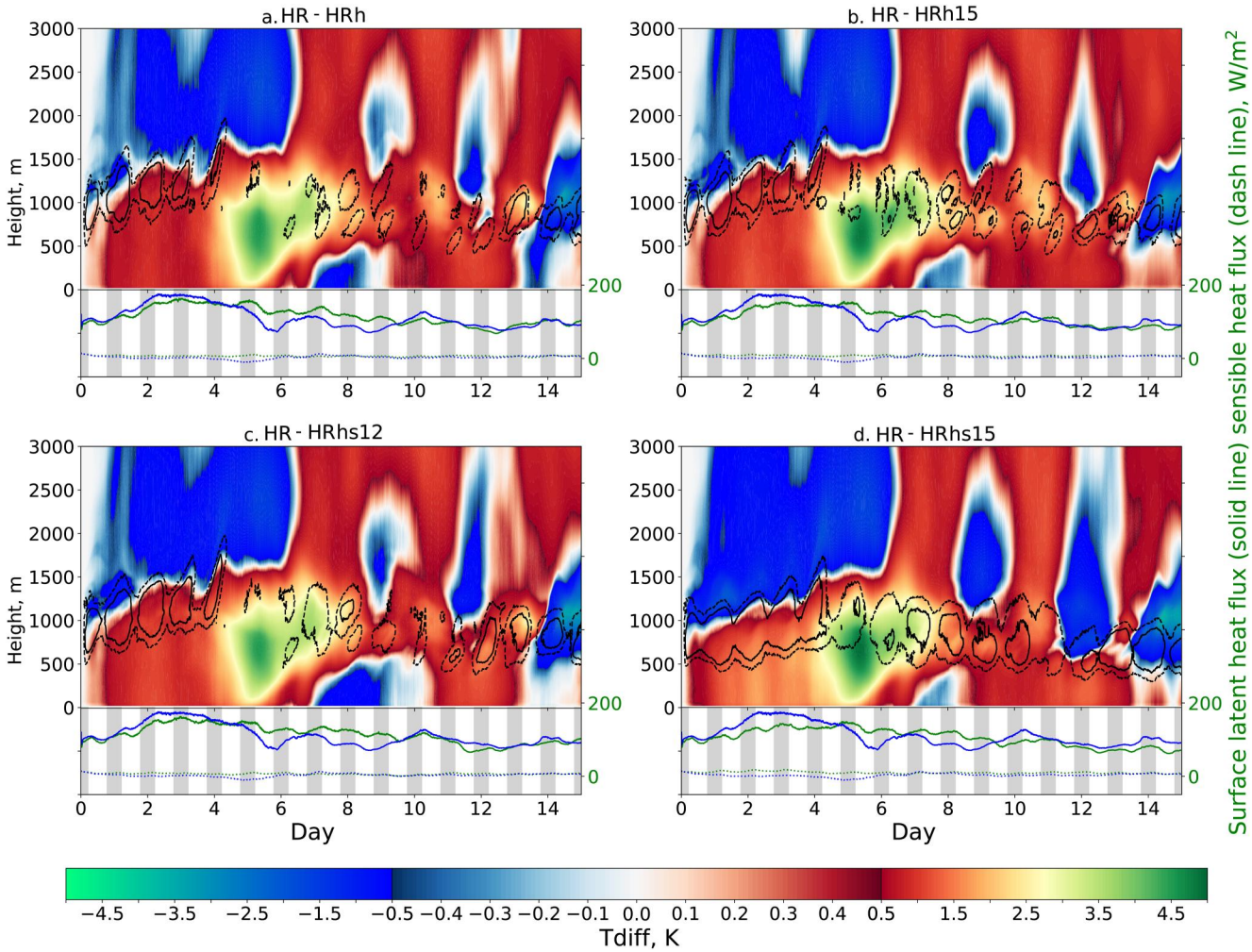

Figure B4. Height time evolution of temperature difference in Namibian between HR and (a) HRh, and (b) HRh15, (c) HRhs12, and (d) HRhs15. Surface sensible and latent heat flux are shown by blue solid and dashed lines for HR (blue) and other configurations (green). Two cloud fraction contour lines are 0.1 (black dotted line) and 0.2 (black solid line).

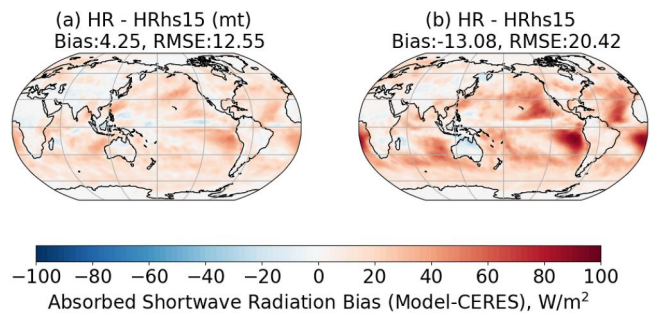

Figure B5. The ASR bias differences between HR and HRhs15 (a) with microphysics tunning and (b) without microphysics tunning.

Data Availability Statement

All E3SM source code can be accessed from the GitHub repository of the E3SM Project, DOE (2018). All code modifications needed to implement our approach within a legacy fork of the E3SM MMF climate model can be

19422466, 2024, 3, Downloaded from https://agupubs.onlinelibrary.wiley.com/doi/10.1029/2023MS003632 by University Of Washington, Wiley Online Library on [25/09/2024]. See the Terms and Conditions (https://onlinelibrary.wiley.com/terms-and-conditions) on Wiley Online Library for rules of use; OA articles are governed by the applicable Creative Commons License

found in the repository of Peng et al. (2023c). The raw output data is archived and can be accessed from Zenodo under the references of Peng et al. (2023a, 2023b).

Acknowledgments

L. Peng, M. Pritchard, P. N. Blossey, and C. S. Bretherton acknowledge funding from the National Science Foundation (NSF) Climate and Large-scale Dynamics program under Grants AGS-1912134 and AGS-1912130. M. Pritchard, L. Peng, and A. M. Jenney further acknowledge DOE BER (DE-SC0023368). The authors acknowledge the Texas Advanced Computing Center (TACC) at The University of Texas at Austin for providing HPC, visualization, database, or grid resources that have contributed to the research results reported within this paper. URL: http://www.tacc.utexas.edu This research was supported by the Exascale Computing Project (17-SC-20-SC), a collaborative effort of the U.S. Department of Energy Office of Science and the National Nuclear Security Administration and by the Energy Exascale Earth System Model (E3SM) project, funded by the U.S. Department of Energy, Office of Science, Office of Biological and Environmental Research. This work was performed under the auspices of the U.S. Department of Energy by Lawrence Livermore National Laboratory under Contract DE-AC52-07NA27344. This research used resources of the Oak Ridge Leadership Computing Facility, which is a DOE Office of Science User Facility supported under Contract DE-AC05-00OR22725.

References

Ackerman, A. S., Stevens, B., Savic-Jovcic, V., Bretherton, C. S., Chlond, A., Golaz, J.-C., et al. (2009). Large-eddy simulations of a drizzling, stratocumulus-topped marine boundary layer. *Monthly Weather Review*, *137*(3), 1083–1110. https://doi.org/10.1175/2008mwr2582.1

Albrecht, B. A., Jensen, M. P., & Syrett, W. J. (1995). Marine boundary layer structure and fractional cloudiness. *Journal of Geophysical Research*, *100*(D7), 14209–14222. https://doi.org/10.1029/95jd00827

Bogenschutz, P. A., Gettelman, A., Morrison, H., Larson, V. E., Craig, C., & Schanen, D. P. (2013). Higher-order turbulence closure and its impact on climate simulations in the community atmosphere model. *Journal of Climate*, *26*(23), 9655–9676. https://doi.org/10.1175/jcli-d-13-00075.1

Bony, S., & Dufresne, J.-L. (2005). Marine boundary layer clouds at the heart of tropical cloud feedback uncertainties in climate models. *Geophysical Research Letters*, *32*(20), L20806. https://doi.org/10.1029/2005gl023851

Bony, S., Webb, M., Bretherton, C., Klein, S., Siebesma, P., Tselioudis, G., & Zhang, M. (2011). CFMIP: Towards a better evaluation and understanding of clouds and cloud feedbacks in CMIP5 models. *Clivar Exchanges*, *56*(2), 20–22.

Bretherton, C. S. (2015). Insights into low-latitude cloud feedbacks from high-resolution models. *Philosophical Transactions of the Royal Society A: Mathematical, Physical & Engineering Sciences*, *373*(2054), 20140415. https://doi.org/10.1098/rsta.2014.0415

Bretherton, C. S., Blossey, P. N., & Uchida, J. (2007). Cloud droplet sedimentation, entrainment efficiency, and subtropical stratocumulus albedo. *Geophysical Research Letters*, *34*(3), L03813. https://doi.org/10.1029/2006gl027648

Bretherton, C. S., MacVean, M. K., Bechtold, P., Chlond, A., Cotton, W. R., Cuxart, J., et al. (1999). An intercomparison of radiatively driven entrainment and turbulence in a smoke cloud, as simulated by different numerical models. *Quarterly Journal of the Royal Meteorological Society*, *125*(554), 391–423. https://doi.org/10.1002/qj.49712555402

Bretherton, C. S., & Wyant, M. C. (1997). Moisture transport, lower-tropospheric stability, and decoupling of cloud-topped boundary layers. *Journal of the Atmospheric Sciences*, *54*(1), 148–167. https://doi.org/10.1175/1520-0469(1997)054<0148:mtltsa>2.0.co;2

Brunke, M. A., Ma, P.-L., Reeves Eyre, J. J., Rasch, P. J., Sorooshian, A., & Zeng, X. (2019). Subtropical marine low stratiform cloud deck spatial errors in the E3SMv1 atmosphere model. *Geophysical Research Letters*, *46*(21), 12598–12607. https://doi.org/10.1029/2019gl084747

Caughey, S., Crease, B., & Roach, W. (1982). A field study of nocturnal stratocumulus ii turbulence structure and entrainment. *Quarterly Journal of the Royal Meteorological Society*, *108*(455), 125–144. https://doi.org/10.1256/smsqj.45507

Cheng, A., & Xu, K.-M. (2015). Improved low-cloud simulation from the community atmosphere model with an advanced third-order turbulence closure. *Journal of Climate*, *28*(14), 5737–5762. https://doi.org/10.1175/jcli-d-14-00776.1

Cohen, Y., Lopez-Gomez, I., Jaruga, A., He, J., Kaul, C. M., & Schneider, T. (2020). Unified entrainment and detrainment closures for extended eddy-diffusivity mass-flux schemes. *Journal of Advances in Modeling Earth Systems*, *12*(9), e2020MS002162. https://doi.org/10.1029/2020ms002162

Dal Gesso, S., Van der Dussen, J., Siebesma, A., De Roode, S., Boutle, I., Kamae, Y., et al. (2015). A single-column model intercomparison on the stratocumulus representation in present-day and future climate. *Journal of Advances in Modeling Earth Systems*, *7*(2), 617–647. https://doi.org/10.1002/2014ms000377

Dodson, D. S., & Small Griswold, J. D. (2021). Turbulent and boundary layer characteristics during VOCALS-REx. *Atmospheric Chemistry and Physics*, *21*(3), 1937–1961. https://doi.org/10.5194/acp-21-1937-2021

Dunbar, O. R., Howland, M. F., Schneider, T., & Stuart, A. M. (2022). Ensemble-based experimental design for targeting data acquisition to inform climate models. *Journal of Advances in Modeling Earth Systems*, *14*(9), e2022MS002997. https://doi.org/10.1029/2022ms002997

E3SM Project, DOE. (2018). Energy exascale Earth system model [Software]. Retrieved from https://github.com/E3SM-Project/E3SM

Eldred, C. (2021). *Structure-preserving numerical discretizations for domains with boundaries*. (Technical Report). Sandia National Laboratories (SNL-NM).

Geoffroy, O., Brenguier, J.-L., & Burnet, F. (2010). Parametric representation of the cloud droplet spectra for les warm bulk microphysical schemes. *Atmospheric Chemistry and Physics*, *10*(10), 4835–4848. https://doi.org/10.5194/acp-10-4835-2010

Gettelman, A., & Sherwood, S. C. (2016). Processes responsible for cloud feedback. *Current Climate Change Reports*, *2*(4), 179–189. https://doi.org/10.1007/s40641-016-0052-8

Golaz, J.-C., Caldwell, P. M., Van Roekel, L. P., Petersen, M. R., Tang, Q., Wolfe, J. D., et al. (2019). The DOE E3SM coupled model version 1: Overview and evaluation at standard resolution. *Journal of Advances in Modeling Earth Systems*, *11*(7), 2089–2129. https://doi.org/10.1029/2018ms001603

Golaz, J.-C., Larson, V. E., & Cotton, W. R. (2002a). A PDF-based model for boundary layer clouds. Part II: Model results. *Journal of the Atmospheric Sciences*, *59*(24), 3552–3571. https://doi.org/10.1175/1520-0469(2002)059<3552:apbmfb>2.0.co;2

Golaz, J.-C., Larson, V. E., & Cotton, W. R. (2002b). A PDF-based model for boundary layer clouds. Part I: Method and model description. *Journal of the Atmospheric Sciences*, *59*(24), 3540–3551. https://doi.org/10.1175/1520-0469(2002)059<3540:apbmfb>2.0.co;2

Grabowski, W. W. (2004). An improved framework for superparameterization. *Journal of the Atmospheric Sciences*, *61*(15), 1940–1952. https://doi.org/10.1175/1520-0469(2004)061<1940:aiffs>2.0.co;2

Haman, K. E., Malinowski, S. P., Kurowski, M. J., Gerber, H., & Brenguier, J.-L. (2007). Small scale mixing processes at the top of a marine stratocumulus—A case study. *Quarterly Journal of the Royal Meteorological Society: A Journal of the Atmospheric Sciences, Applied Meteorology and Physical Oceanography*, *133*(622), 213–226. https://doi.org/10.1002/qj.5

Hannah, W., & Pressel, K. (2022). Transporting CRM variance in a multiscale modelling framework. *EGUsphere*, *2022*, 1–25. https://doi.org/10.5194/egusphere-2022-397

Hannah, W. M., Bradley, A. M., Guba, O., Tang, Q., Golaz, J.-C., & Wolfe, J. (2021). Separating physics and dynamics grids for improved computational efficiency in spectral element Earth system models. *Journal of Advances in Modeling Earth Systems*, *13*(7), e2020MS002419. https://doi.org/10.1029/2020ms002419

Hannah, W. M., Jones, C. R., Hillman, B. R., Norman, M. R., Bader, D. C., Taylor, M. A., et al. (2020). Initial results from the super-parameterized E3SM. *Journal of Advances in Modeling Earth Systems*, *12*(1). https://doi.org/10.1029/2019ms001863

Heinze, R., Mironov, D., & Raasch, S. (2015). Second-moment budgets in cloud topped boundary layers: A large-eddy simulation study. *Journal of Advances in Modeling Earth Systems*, *7*(2), 510–536. https://doi.org/10.1002/2014ms000376

Hersbach, H., Bell, B., Berrisford, P., Hirahara, S., Horányi, A., Muñoz-Sabater, J., et al. (2020). The ERA5 global reanalysis. *Quarterly Journal of the Royal Meteorological Society*, *146*(730), 1999–2049. https://doi.org/10.1002/qj.3803

19422466, 2024, 3, Downloaded from https://agupubs.onlinelibrary.wiley.com/doi/10.1029/2023MS003632 by University Of Washington, Wiley Online Library on [25/09/2024]. See the Terms and Conditions (https://onlinelibrary.wiley.com/terms-and-conditions) on Wiley Online Library for rules of use; OA articles are governed by the applicable Creative Commons License

Heymsfield, A. J. (2003). Properties of tropical and midlatitude ice cloud particle ensembles. Part II: Applications for mesoscale and climate models. *Journal of the Atmospheric Sciences*, *60*(21), 2592–2611. https://doi.org/10.1175/1520-0469(2003)060<2592:potami>2.0.co;2

Hignett, P. (1991). Observations of diurnal variation in a cloud-capped marine boundary layer. *Journal of the Atmospheric Sciences*, *48*(12), 1474–1482. https://doi.org/10.1175/1520-0469(1991)048<1474:oodvia>2.0.co;2

Hurrell, J. W., Holland, M. M., Gent, P. R., Ghan, S., Kay, J. E., Kushner, P. J., et al. (2013). The community Earth system model: A framework for collaborative research. *Bulletin of the American Meteorological Society*, *94*(9), 1339–1360. https://doi.org/10.1175/BAMS-D-12-00121.1

Jansson, F., Van Den Oord, G., Pelupessy, I., Chertova, M., Grönqvist, J. H., Siebesma, A. P., & Crommelin, D. (2022). Representing cloud mesoscale variability in superparameterized climate models. *Journal of Advances in Modeling Earth Systems*, *14*(8), e2021MS002892. https://doi.org/10.1029/2021ms002892

Jones, C. R., Bretherton, C. S., & Pritchard, M. S. (2015). Mean-state acceleration of cloud-resolving models and large eddy simulations. *Journal of Advances in Modeling Earth Systems*, *7*(4), 1643–1660. https://doi.org/10.1002/2015MS000488

Khairoutdinov, M., Randall, D., & DeMott, C. (2005). Simulations of the atmospheric general circulation using a cloud-resolving model as a superparameterization of physical processes. *Journal of the Atmospheric Sciences*, *62*(7), 2136–2154. https://doi.org/10.1175/jas3453.1

Khairoutdinov, M. F., & Randall, D. A. (2001). A cloud resolving model as a cloud parameterization in the NCAR community climate system model: Preliminary results. *Geophysical Research Letters*, *28*(18), 3617–3620. https://doi.org/10.1029/2001gl013552

Khairoutdinov, M. F., & Randall, D. A. (2003). Cloud resolving modeling of the ARM summer 1997 IOP: Model formulation, results, uncertainties, and sensitivities. *Journal of the Atmospheric Sciences*, *60*(4), 607–625. https://doi.org/10.1175/1520-0469(2003)060<0607:crmota>2.0.co;2

Konsta, D., Dufresne, J.-L., Chepfer, H., Vial, J., Koshiro, T., Kawai, H., et al. (2022). Low-level marine tropical clouds in six CMIP6 models are too few, too bright but also too compact and too homogeneous. *Geophysical Research Letters*, *49*(11), e2021GL097593. https://doi.org/10.1029/2021gl097593

Kooperman, G. J., Pritchard, M. S., Burt, M. A., Branson, M. D., & Randall, D. A. (2016a). Impacts of cloud superparameterization on projected daily rainfall intensity climate changes in multiple versions of the community Earth system model. *Journal of Advances in Modeling Earth Systems*, *8*(4), 1727–1750. https://doi.org/10.1002/2016ms000715

Kooperman, G. J., Pritchard, M. S., Burt, M. A., Branson, M. D., & Randall, D. A. (2016b). Robust effects of cloud superparameterization on simulated daily rainfall intensity statistics across multiple versions of the community Earth system model. *Journal of Advances in Modeling Earth Systems*, *8*(1), 140–165. https://doi.org/10.1002/2015ms000574

Larson, V. E., & Golaz, J.-C. (2005). Using probability density functions to derive consistent closure relationships among higher-order moments. *Monthly Weather Review*, *133*(4), 1023–1042. https://doi.org/10.1175/mwr2902.1

Larson, V. E., Schanen, D. P., Wang, M., Ovchinnikov, M., & Ghan, S. (2012). PDF parameterization of boundary layer clouds in models with horizontal grid spacings from 2 to 16 km. *Monthly Weather Review*, *140*(1), 285–306. https://doi.org/10.1175/mwr-d-10-05059.1

Lee, H.-H., Bogenschutz, P., & Yamaguchi, T. (2022). Resolving away stratocumulus biases in modern global climate models. *Geophysical Research Letters*, *49*(18), e2022GL099422. https://doi.org/10.1029/2022gl099422

Lilly, D. K. (1968). Models of cloud-topped mixed layers under a strong inversion. *Quarterly Journal of the Royal Meteorological Society*, *94*(401), 292–309. https://doi.org/10.1002/qj.49709440106

Lin, J.-L., Qian, T., & Shinoda, T. (2014). Stratocumulus clouds in southeastern Pacific simulated by eight CMIP5–CFMIP global climate models. *Journal of Climate*, *27*(8), 3000–3022. https://doi.org/10.1175/jcli-d-13-00376.1

Lopez-Gomez, I., Cohen, Y., He, J., Jaruga, A., & Schneider, T. (2020). A generalized mixing length closure for eddy-diffusivity mass-flux schemes of turbulence and convection. *Journal of Advances in Modeling Earth Systems*, *12*(11), e2020MS002161. https://doi.org/10.1029/2020ms002161

Maron, J. L., Mac Low, M.-M., & Oishi, J. S. (2008). A constrained-transport magnetohydrodynamics algorithm with near-spectral resolution. *The Astrophysical Journal*, *677*(1), 520–529. https://doi.org/10.1086/525011

Mechem, D. B., Yuter, S. E., & De Szoeke, S. P. (2012). Thermodynamic and aerosol controls in southeast Pacific stratocumulus. *Journal of the Atmospheric Sciences*, *69*(4), 1250–1266. https://doi.org/10.1175/jas-d-11-0165.1

Mellado, J. P. (2017). Cloud-top entrainment in stratocumulus clouds. *Annual Review of Fluid Mechanics*, *49*(1), 145–169. https://doi.org/10.1146/annurev-fluid-010816-060231

Miller, M. A., Jensen, M. P., & Clothiaux, E. E. (1998). Diurnal cloud and thermodynamic variations in the stratocumulus transition regime: A case study using in situ and remote sensors. *Journal of the Atmospheric Sciences*, *55*(13), 2294–2310. https://doi.org/10.1175/1520-0469(1998)055<2294:dcatvi>2.0.co;2

Miyamoto, Y., Kajikawa, Y., Yoshida, R., Yamaura, T., Yashiro, H., & Tomita, H. (2013). Deep moist atmospheric convection in a subkilometer global simulation. *Geophysical Research Letters*, *40*(18), 4922–4926. https://doi.org/10.1002/grl.50944

Moeng, C.-H., Cotton, W., Bretherton, C., Chlond, A., Khairoutdinov, M., Krueger, S., et al. (1996). Simulation of a stratocumulus-topped planetary boundary layer: Intercomparison among different numerical codes. *Bulletin of the American Meteorological Society*, *77*(2), 261–278. https://doi.org/10.1175/1520-0477(1996)077<0261:soastp>2.0.co;2

Morrison, H., & Milbrandt, J. A. (2015). Parameterization of cloud microphysics based on the prediction of bulk ice particle properties. Part I: Scheme description and idealized tests. *Journal of the Atmospheric Sciences*, *72*(1), 287–311. https://doi.org/10.1175/jas-d-14-0065.1

Muller, C. J., & Held, I. M. (2012). Detailed investigation of the self-aggregation of convection in cloud-resolving simulations. *Journal of the Atmospheric Sciences*, *69*(8), 2551–2565. https://doi.org/10.1175/jas-d-11-0257.1

Nicholls, S. (1989). The structure of radiatively driven convection in stratocumulus. *Quarterly Journal of the Royal Meteorological Society*, *115*(487), 487–511. https://doi.org/10.1256/smsqj.48703

Norman, M. R., Bader, D., Hannah, W., Hillman, B., Jones, C. R., Leung, R. L., et al. (2019). Unprecedented cloud resolution in a GPU-enabled full-physics atmospheric climate simulation on OLCF's summit supercomputer.

Parishani, H., Pritchard, M. S., Bretherton, C. S., Terai, C. R., Wyant, M. C., Khairoutdinov, M., & Singh, B. (2018). Insensitivity of the cloud response to surface warming under radical changes to boundary layer turbulence and cloud microphysics: Results from the ultraparameterized CAM. *Journal of Advances in Modeling Earth Systems*, *10*(12), 3139–3158. https://doi.org/10.1029/2018ms001409

Parishani, H., Pritchard, M. S., Bretherton, C. S., Wyant, M. C., & Khairoutdinov, M. (2017). Toward low-cloud-permitting cloud superparameterization with explicit boundary layer turbulence. *Journal of Advances in Modeling Earth Systems*, *9*(3), 1542–1571. https://doi.org/10.1002/2017ms000968

Park, S., Leovy, C. B., & Rozendaal, M. A. (2004). A new heuristic Lagrangian marine boundary layer cloud model. *Journal of the Atmospheric Sciences*, *61*(24), 3002–3024. https://doi.org/10.1175/jas-3344.1

19422466, 2024, 3, Downloaded from https://agupubs.onlinelibrary.wiley.com/doi/10.1029/2023MS003632 by University Of Washington, Wiley Online Library on [25/09/2024]. See the Terms and Conditions (https://onlinelibrary.wiley.com/terms-and-conditions) on Wiley Online Library for rules of use; OA articles are governed by the applicable Creative Commons License

Peng, L., Pritchard, M., Blossey, P. N., Hannah, W. M., Bretherton, C. S., Terai, C. R., & Jenney, A. M. (2023a). Improving stratocumulus cloud amounts in a 200-m resolution multi-scale modeling framework through tuning of its interior physics part 1 [Dataset]. Zenodo. https://doi.org/10.5281/zenodo.7516620

Peng, L., Pritchard, M., Blossey, P. N., Hannah, W. M., Bretherton, C. S., Terai, C. R., & Jenney, A. M. (2023b). Improving stratocumulus cloud amounts in a 200-m resolution multi-scale modeling framework through tuning of its interior physics part 2 [Dataset]. Zenodo. https://doi.org/10.5281/zenodo.7517514

Peng, L., Pritchard, M., Blossey, P. N., Hannah, W. M., Bretherton, C. S., Terai, C. R., & Jenney, A. M. (2023c). Modified energy exascale Earth system model with hyperviscosity and sedimentation [Software]. https://github.com/liranpeng/E3SM-omp4.5/tree/Hyperviscosity_Sedimentation

Peng, L., Pritchard, M., Hannah, W. M., Blossey, P. N., Worley, P. H., & Bretherton, C. S. (2022). Load-balancing intense physics calculations to embed regionalized high-resolution cloud resolving models in the E3SM and CESM climate models. *Journal of Advances in Modeling Earth Systems*, *14*(5), e2021MS002841. https://doi.org/10.1029/2021ms002841

Pincus, R., Mlawer, E. J., & Delamere, J. S. (2019). Balancing accuracy, efficiency, and flexibility in radiation calculations for dynamical models. *Journal of Advances in Modeling Earth Systems*, *11*(10), 3074–3089. https://doi.org/10.1029/2019ms001621

Pressel, K. G., Mishra, S., Schneider, T., Kaul, C. M., & Tan, Z. (2017). Numerics and subgrid-scale modeling in large eddy simulations of stratocumulus clouds. *Journal of Advances in Modeling Earth Systems*, *9*(2), 1342–1365. https://doi.org/10.1002/2016ms000778

Randall, D., Coakley, J., Fairall, C., Knopfli, R., & Lenschow, D. (1984). Outlook for research on marine subtropical stratocumulus clouds. *Bulletin of the American Meteorological Society*, *65*(12), 1290–1301. https://doi.org/10.1175/1520-0477(1984)065<1290:ofrosm>2.0.co;2

Ronchi, C., Iacono, R., & Paolucci, P. S. (1996). The "cubed sphere": A new method for the solution of partial differential equations in spherical geometry. *Journal of Computational Physics*, *124*(1), 93–114. https://doi.org/10.1006/jcph.1996.0047

Schneider, T., Lan, S., Stuart, A., & Teixeira, J. (2017). Earth system modeling 2.0: A blueprint for models that learn from observations and targeted high-resolution simulations. *Geophysical Research Letters*, *44*(24), 12–396. https://doi.org/10.1002/2017gl076101

Stevens, B., Acquistapace, C., Hansen, A., Heinze, R., Klinger, C., Klocke, D., et al. (2020). The added value of large-eddy and storm-resolving models for simulating clouds and precipitation. *Journal of the Meteorological Society of Japan. Ser. II*, *98*(2), 395–435. https://doi.org/10.2151/jmsj.2020-021

Stevens, B., Moeng, C.-H., Ackerman, A. S., Bretherton, C. S., Chlond, A., de Roode, S., et al. (2005). Evaluation of large-eddy simulations via observations of nocturnal marine stratocumulus. *Monthly Weather Review*, *133*(6), 1443–1462. https://doi.org/10.1175/mwr2930.1

Taylor, M., Edwards, J., Thomas, S., & Nair, R. (2007). A mass and energy conserving spectral element atmospheric dynamical core on the cubed-sphere grid. In *Journal of physics: Conference series* (Vol. 78, p. 012074).

Tselioudis, G., Rossow, W. B., Jakob, C., Remillard, J., Tropf, D., & Zhang, Y. (2021). Evaluation of clouds, radiation, and precipitation in CMIP6 models using global weather states derived from ISCCP-H cloud property data. *Journal of Climate*, *34*(17), 7311–7324. https://doi.org/10.1175/jcli-d-21-0076.1

Tsushima, Y., Ringer, M. A., Koshiro, T., Kawai, H., Roehrig, R., Cole, J., et al. (2016). Robustness, uncertainties, and emergent constraints in the radiative responses of stratocumulus cloud regimes to future warming. *Climate Dynamics*, *46*(9), 3025–3039. https://doi.org/10.1007/s00382-015-2750-7

Tulich, S. (2015). A strategy for representing the effects of convective momentum transport in multiscale models: Evaluation using a new superparameterized version of the weather research and forecast model (SP-WRF). *Journal of Advances in Modeling Earth Systems*, *7*(2), 938–962. https://doi.org/10.1002/2014ms000417

van Zanten, M. C. (2002). Radiative and evaporative cooling in the entrainment zone of stratocumulus–the role of longwave radiative cooling above cloud top. *Boundary-Layer Meteorology*, *102*(2), 253–280. https://doi.org/10.1023/a:1013129713315

Vignesh, P. P., Jiang, J. H., Kishore, P., Su, H., Smay, T., Brighton, N., & Velicogna, I. (2020). Assessment of CMIP6 cloud fraction and comparison with satellite observations. *Earth and Space Science*, *7*(2), e2019EA000975. https://doi.org/10.1029/2019ea000975

Wang, M., Larson, V. E., Ghan, S., Ovchinnikov, M., Schanen, D. P., Xiao, H., et al. (2015). A multiscale modeling framework model (superparameterized CAM5) with a higher-order turbulence closure: Model description and low-cloud simulations. *Journal of Advances in Modeling Earth Systems*, *7*(2), 484–509. https://doi.org/10.1002/2014ms000375

Webb, M. J., Lambert, F. H., & Gregory, J. M. (2013). Origins of differences in climate sensitivity, forcing and feedback in climate models. *Climate Dynamics*, *40*(3), 677–707. https://doi.org/10.1007/s00382-012-1336-x

Wicker, L. J., & Skamarock, W. C. (2002). Time-splitting methods for elastic models using forward time schemes. *Monthly Weather Review*, *130*(8), 2088–2097. https://doi.org/10.1175/1520-0493(2002)130<2088:tsmfem>2.0.co;2

Williams, K. D., Bodas-Salcedo, A., Déqué, M., Fermepin, S., Medeiros, B., Watanabe, M., et al. (2013). The transpose-AMIP II experiment and its application to the understanding of southern ocean cloud biases in climate models. *Journal of Climate*, *26*(10), 3258–3274. https://doi.org/10.1175/jcli-d-12-00429.1

Wood, R. (2012). Stratocumulus clouds. *Monthly Weather Review*, *140*(8), 2373–2423. https://doi.org/10.1175/mwr-d-11-00121.1

Wyant, M. C., Bretherton, C. S., & Blossey, P. N. (2018). The sensitivity of numerical simulations of cloud-topped boundary layers to cross-grid flow. *Journal of Advances in Modeling Earth Systems*, *10*(2), 466–480. https://doi.org/10.1002/2017ms001241

Xie, S., Lin, W., Rasch, P. J., Ma, P.-L., Neale, R., Larson, V. E., et al. (2018). Understanding cloud and convective characteristics in version 1 of the E3SM atmosphere model. *Journal of Advances in Modeling Earth Systems*, *10*(10), 2618–2644. https://doi.org/10.1029/2018MS001350

Yang, Q., Hannah, W. M., & Leung, L. R. (2022). Convective momentum transport and its impact on the Madden-Julian oscillation in E3SM-MMF. *Journal of Advances in Modeling Earth Systems*, *14*(11), e2022MS003206. https://doi.org/10.1029/2022ms003206

Yau, M. K., & Rogers, R. R. (1996). *A short course in cloud physics*. Elsevier.

Zelinka, M. D., Klein, S. A., Qin, Y., & Myers, T. A. (2022). Evaluating climate models' cloud feedbacks against expert judgment. *Journal of Geophysical Research: Atmospheres*, *127*(2), e2021JD035198. https://doi.org/10.1029/2021jd035198

Zelinka, M. D., Myers, T. A., McCoy, D. T., Po-Chedley, S., Caldwell, P. M., Ceppi, P., et al. (2020). Causes of higher climate sensitivity in CMIP6 models. *Geophysical Research Letters*, *47*(1), e2019GL085782. https://doi.org/10.1029/2019gl085782

19422466, 2024, 3, Downloaded from https://agupubs.onlinelibrary.wiley.com/doi/10.1029/2023MS003632 by University Of Washington, Wiley Online Library on [25/09/2024]. See the Terms and Conditions (https://onlinelibrary.wiley.com/terms-and-conditions) on Wiley Online Library for rules of use; OA articles are governed by the applicable Creative Commons License